Climate Dynamics
https://doi.org/10.1007/s00382-017-4021-2

Modulation of ENSO evolution by strong tropical volcanic eruptions

Tao Wang[1,2] · Dong Guo[3] · Yongqi Gao[1,4] · Huijun Wang[1,2,5] · Fei Zheng[2,6] · Yali Zhu[1,2] · Jiapeng Miao[1,7] · Yongyun Hu[8]

Received: 9 July 2017 / Accepted: 18 November 2017
© Springer-Verlag GmbH Germany, part of Springer Nature 2017

Abstract
The simulated responses of the El Niño–Southern Oscillation (ENSO) to volcanic forcings are controversial, and some mechanisms of these responses are not clear. We investigate the impacts of volcanic forcing on the ENSO using a long-term simulation covering 1400–1999 as simulated by the Bergen Climate Model (BCM) and a group of simulations performed with the Community Atmosphere Model version 4.0 (CAM4) and the BCM's ocean component Miami Isopycanic Coordinated Ocean Model (MICOM). The analysis of the long-term BCM simulation indicates that ENSO has a negative-positive-negative response to strong tropical volcanic eruptions (SVEs), which corresponds to the different stages of volcanic forcing. In the initial forcing stage, a brief and weak La Niña-like response is caused by the cooling along the west coast of the South American continent and associated enhancement of the trade winds. In the peak forcing stage, westerly wind anomalies are excited by both reduced east–west sea level pressure gradients and weakened and equatorward shifted tropical convergence zones. These westerly wind anomalies extend to the equatorial eastern Pacific, leading to an El Niño-like response. At the same time, easterly wind anomalies west of 120°E and strong cooling effects can promote a discharged thermocline state and excite an upwelling Kelvin wave in the western Pacific. In the declining forcing stage, forced by the recovered trade winds, the upwelling Kelvin wave propagates eastward and reaches the equatorial eastern Pacific. Through the Bjerknes feedback, a strong and temporally extended La Niña-like response forms. Additional CAM4 simulations suggest a more important role of the surface cooling over the Maritime Continent and surrounding ocean in shaping the westerly wind anomalies over the equatorial central-eastern Pacific and the easterly wind anomalies west of 120° E, which are key to causing the El Niño-like responses and subsequent La Niña-like responses, respectively. The MICOM sensitivity simulations confirm that SVE-induced tropical atmospheric circulation anomalies play a dominant role in regulating post-eruption ENSO evolution in the observation, while the influences of anomalous buoyance forcing (heat and freshwater fluxes) are secondary. Therefore, SVEs play an important role in modulating the ENSO evolution. Compared with proxy data, the simulated El Niño-like responses and subsequent La Niña-like responses are consistent with the reconstructed ENSO responses to SVEs. However, the simulated initial brief La Niña-like response, which is reproduced by most models, is seen in only one proxy dataset and is absent in most of the reconstructed ENSOs and those observed. The reason for this model-data mismatch will require further investigation.

Keywords Strong tropical volcanic eruption · El Niño–Southern Oscillation · Trade winds · Model · Kelvin wave

1 Introduction

The El Niño–Southern Oscillation (ENSO) is a coupled ocean–atmosphere phenomenon with annual and inter-annual timescales. It features an irregular inter-annual oscillation between warmer (El Niño) and colder (La Niña) sea surface temperatures (SST) in the tropical Pacific (Latif et al. 1998; McPhaden et al. 2006). Although ENSO originates and develops in the tropical Pacific, its influence covers not only the Pacific but also the global climate at seasonal to

Electronic supplementary material The online version of this article (https://doi.org/10.1007/s00382-017-4021-2) contains supplementary material, which is available to authorized users.

✉ Tao Wang
wangtao@mail.iap.ac.cn

Extended author information available on the last page of the article

Published online: 23 November 2017

inter-annual scales. For example, ENSO is suggested to have a significant influence on the East Asian monsoons (e.g., Zhang et al. 1999; Chang et al. 2000; Chen et al. 2007; Zhou and Chan 2007; Zhou et al. 2007; Gu et al. 2010), the European climate (e.g., Fraedrich 1994; Moron and Plaut 2003; Brönnimann 2007; Graf et al. 2014), the rainfall extremes in South and North America (e.g., Cayan et al. 1999; Andreoli and Kayano 2005), the Australian rainfall variability (e.g., Cai and Cowan 2009; Cai et al. 2011) and the recent slowdown of global warming (Kosaka and Xie 2013). Furthermore, ENSO can also modulate the Pacific Decadal Oscillation (Newman et al. 2003; Zanchettin et al. 2016) and the dominant component of the tropical variability on an intraseasonal time scale: the Madden–Julian Oscillation (Chen et al. 2016).

The ENSO cycle includes its initiation, development, and decay phases. Bjerknes (1969) was the first to hypothesize that an initial positive SST anomaly in the eastern equatorial Pacific could lead to El Niño through a positive ocean–atmosphere feedback. Later, four major negative feedbacks were proposed to turn the initial warm state into ENSO-like oscillations (Wang and Picaut 2004). The proposed frameworks include the delayed oscillator (Suarez and Schopf 1988; Battisti and Hirst 1989), the recharge oscillator (Jin 1997a, b), the western Pacific oscillator (Weisberg and Wang 1997; Wang et al. 1999), and the advective-reflective oscillator (Picaut et al. 1997). Further, Neelin et al. (1998) and Picaut et al. (2002) suggested that additional mechanisms should be proposed for ENSO's irregularity, including interactions with the seasonal cycle, chaotic behavior, long-term natural and anthropogenic variations, and high-frequency forcings such as westerly wind bursts.

Depending on the spatial and temporal evolutions of the SST anomalies over the tropical Pacific, El Niño events can be classified as eastern Pacific El Niño or central Pacific El Niño events. The canonical El Niño usually refers to eastern Pacific El Niño events, involving the westward propagation of positive SST anomalies off the South American coast in the eastern Pacific (Rasmusson and Carpenter 1982). Recently, central Pacific El Niño events have been documented as a new type or, alternatively, an increasingly recurrent type of El Niño (e.g., Ashok et al. 2007; Kao and Yu 2009; Pascolini-Campbell et al. 2015). These events are characterized by positive SST anomalies in the central tropical Pacific flanked by negative SST anomalies to the west and east. Thus, ENSO and its related mechanisms are diverse (Zhang et al. 2007; Giese and Ray 2011; Johnson 2013; Chen et al. 2015). In general, the subsurface oceanic temperature anomaly in the western Pacific and the cumulative zonal wind anomalies over the tropical Pacific play key roles in ENSO evolution (Lai et al. 2015). Other factors, such as anomalous freshwater fluxes affecting sea surface salinity and related oceanic processes (Yang et al. 1999; Zhang and Busalacchi 2009; Zheng and Zhang 2012) and oceanic biologically-induced heating (Chavez et al. 1999; Timmermann and Jin 2002; Marzeion et al. 2005; Zhang et al. 2015), have also been suggested to influence ENSO.

External forcings may play important roles in the regulation of ENSO. For example, greenhouse gas-induced global warming favors more frequent extreme El Niño and La Niña events based on the modeling results from the Coupled Model Intercomparison Project Phase 3 and 5 (CMIP3 and CMIP5) (Cai et al. 2014, 2015a). Changes in incoming solar radiation affect the heat budget of the equatorial Pacific Ocean and, consequently, ENSO (Lewis et al. 1990; Liu et al. 2015).

Volcanic eruptions are another important external forcing that impacts regional and global climates (Robock 2000). Volcanic aerosols cool the troposphere and surface by scattering and reflecting solar radiation as well as warming the stratosphere by absorbing terrestrial radiation. Significant changes have been found in the global and regional surface air temperatures and precipitations following volcanic eruptions, especially following strong tropical volcanic eruptions (SVEs) (e.g., Robock and Mao 1995; Stenchikov et al. 1998; Trenberth and Dai 2007; Otterå 2008; Liu et al. 2016). Volcanic eruptions can impact monsoons (e.g., Peng et al. 2010; Cui et al. 2014; Miao et al. 2016; Zambri and Robock 2016) and modulate the decadal to multidecadal climate variability over the Northern Hemisphere (Otterå et al. 2010; Wang et al. 2012; Zanchettin et al. 2012; Zanchettin 2017).

For ENSO, Adams et al. (2003) revealed a close connection between strong volcanic eruptions and subsequent El Niño events by analyzing paleoclimate reconstructions of ENSO and suggested a rebound from volcanism-induced El Niño-like conditions into La Niña-like states. Liu et al. (2017) drew the same conclusion based on ten ENSO reconstructions. However, there is also proxy evidence indicating an immediate La Niña-like tropical Pacific cooling, prior to the El Niño-like response of the eruption year (Li et al. 2013).

Numerical models have also been used to investigate the responses of ENSO to volcanic forcing. For instance, Mann et al. (2005) used the Zebiak-Cane model (Zebiak and Cane 1987) and found an El Niño-like SST anomaly response to the prescribed spatially-uniform distribution of surface cooling over the tropical Pacific. Subsequently, global coupled ocean–atmosphere models are used to further explore the responses of ENSO to volcanic eruptions. Emile-Geay et al. (2008) suggested that volcanic eruptions can increase the likelihoods of El Niño events by an average of 50% via a dynamical thermostat mechanism (Clement et al. 1996; Cane et al. 1997). Ohba et al. (2013) suggested that the intensity of a dynamical thermostat-like response to a SVE could be dependent on the concurrent phase of ENSO. Lim et al. (2016) suggested that

El Niño-like warming occurs when volcanic forcing is above 15 W m^{-2}. In addition, this modeled El Niño-like response is attributed to westerly wind anomalies, which can be excited by stronger coolings over the Maritime Continent (Ohba et al. 2013), an equatorward-shifted and weakened Inter-tropical Convergence Zone (ITCZ) (e.g., Pausata et al. 2015; Lim et al. 2016; Liu et al. 2017), subtropical precipitation increase and associated diabatic heating anomaly (Liu et al. 2017), as well as a stronger cooling over tropical Africa and related atmospheric Kelvin wave (Khodri et al. 2017) based on some recent modeling studies. In contrast, this cause/effect relationship between eruptions and El Niño-like responses is weak in some coupled model (Ding et al. 2014). A La Niña-like response even has been reported by some modeling studies (e.g., McGregor and Timmermann 2011; Zanchettin et al. 2012). The La Niña-like response in some of these modeling studies is identified probably due to the overarching tropical cooling caused by the volcanic forcing, rather than an actual negative ENSO response (Khodri et al. 2017). Nevertheless, some discrepancies in the response of ENSO to SVEs still exist between the different modeling studies. And the main mechanisms for ENSO to responding to volcanic forcing are under debate.

Additionally, more attention has been paid to the response of ENSO during the eruption and the first post-eruption years (i.e., the El Niño-like response in the proxy data-based studies and most modeling studies), rather than to a long-term continuous response. The mechanism for subsequent La Niña-like responses in the second to third post-eruption years, which are also proposed to exist in the ENSO reconstructions, is still not clear. Therefore, many issues surrounding ENSO's response to volcanic forcing remain open to dispute.

In this study, we investigated the responses of the tropical Pacific Ocean to SVEs using observational data, a coupled climate model, an ocean general circulation model (OGCM) and an atmospheric general circulation model (AGCM). In particular, we focus on the impacts of SVEs on ENSO evolution and the associated physical processes during several post-eruption years. The rest of this paper is organized as follows: Sect. 2 describes the model, data, and numerical experiments employed in this study. In Sect. 3, the response of a simulated ENSO to SVEs, and the associated mechanism are investigated using a coupled climate model and an AGCM. In Sect. 4, the ENSO evolutions following three SVEs in the second half of the twentieth century are studied in detail using observations and specifically designed OGCM simulations. The conclusions and discussion are presented in Sect. 5.

2 Model, data, and experiments

The Bergen Climate Model version 2 (hereafter abbreviated as BCM) is a fully coupled atmosphere–ocean–sea-ice general circulation model (Otterå et al. 2010). Its atmospheric component is ARPEGE, a spectral AGCM with a truncation at wavenumber 63 (approximately 2.8° in latitude and longitude). A total of 31 vertical levels ranging from the surface to 10 hPa are employed in the model. The oceanic component is MICOM (Bleck et al. 1992), a global isopycnic coordinate ocean model. It has a general horizontal grid spacing of 2.4° × 2.4° that gradually decreases to 0.8° toward the equator to better resolve the dynamics and has a stack of 34 vertical isopycnic layers. The sea-ice component is the dynamic-thermodynamic sea-ice model GELATO (Salas-Melia 2002). These components are coupled with the OASIS coupler (version 22).

One 600-year long simulation from the BCM is used to investigate the impact of SVEs on the ENSO evolution and the associated mechanisms in the couple model. The 600-year long simulation (hereafter referred to as EXT600) is forced by natural forcings, including changes in the amount of stratospheric aerosols following volcanic eruptions (Fig. 1) and variations in total solar irradiance (Crowley et al. 2003). The anthropogenic forcings, including well-mixed greenhouse gases and tropospheric sulfate aerosols, are fixed at preindustrial (1850) levels. The volcanic aerosol loading in BCM is described as the monthly optical depths at 0.55 microns in the middle of the visible spectrum in four latitude bands (30°N–90°°N, 0–30°N, 30°S–0, 90°S–30°S) (Crowley et al. 2003). The sulfate aerosol loading is distributed throughout all model levels in the stratosphere. The BCM has been shown to well reproduce the current climate (Wang et al. 2013) and the main observed features following the Pinatubo eruption of 1991 (Otterå 2008).

At the same time, an AGCM, the Community Atmosphere Model version 4.0 (CAM4), is used to examine the tropical atmospheric responses to SVE-induced surface cooling in the BCM EXT600 simulation. CAM4 is the atmospheric component of the Community Earth System Model (Gent et al. 2011). In this study, CAM4 has a horizontal grid resolution of 1.9° in latitude by 2.5° in longitude and 26 vertical layers. Details for the CAM4 experiments will be presented in Sect. 3.

In addition to the BCM and CAM4 simulations, we also used the MICOM simulation (from January 1, 1948 to December 31, 2008), which is forced by the daily NCEP–NCAR (the National Centers for Environmental Prediction/National Center for Atmospheric Research) reanalysis dataset (Kalnay et al. 1996). MICOM is integrated for 305 years (five cycles of 1948–2008, with the end of

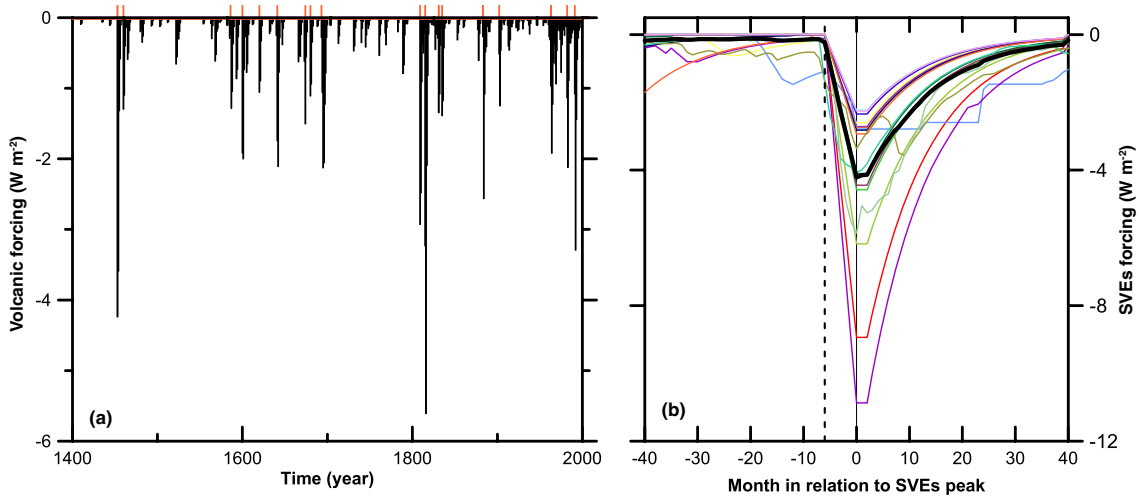

Fig. 1 **a** Global and annual mean volcanic forcing (Crowley et al. 2003) used in the BCM. Orange bars stand for the eighteen SVEs; **b** Tropical (30°S–30°N) averaged monthly volcanic forcing for the eighteen SVEs (color curves) and their mean values (black curve); the solid vertical line stands for the peak time of the SVEs, the dashed vertical line stands for the average eruption start time

the previous cycle used as the initial state of the current cycle), which is a general approach for the ocean model's spin-up (He et al. 2016). The final cycle is used in this study (hereafter abbreviated as MICOM60). To investigate the main mechanism influencing the observed ENSO evolution responses to SVEs, we have performed additional MICOM simulations. The detailed experimental setup can be found in Sect. 4.

The observed SST is from the Hadley Center Monthly Sea Surface Temperature data set (HadISST, Rayner et al. 2003). For statistical analyses, the superposed epoch analysis (SEA, Mitchell 1961; Robock and Mao 1995) and composite analysis are applied to examine the volcanic signals and their associated influences on the tropical Pacific. Following the works of Anchukaitis et al. (2010) and Liu et al. (2016), in the SEA, we normalize the data by the largest absolute anomaly magnitude in an 11-years window (5 years before and 6 years after the SVEs) to avoid any single eruption dominating the epochal signal. A standard Monte Carlo randomization procedure (with a total of 10,000 Monte Carlo simulations) and a standard *t* test are used to determine the statistical significances of the SEA and the composite analysis, respectively.

3 Responses of ENSO cycles to SVEs in the BCM

3.1 Simulated ENSO mode

We use two indices to examine the evolutions of ENSO following SVEs in the EXT600. The first one is the Niño 3.4 SST index (hereafter abbreviated as SST ENSO index), which is defined as the deseasonalized area-averaged monthly SST anomaly from 5°S–5°N and 170°–120°W. The second index is defined as the deseasonalized area-averaged monthly sea surface height (SSH) anomalies over the Niño 3.4 region (hereafter abbreviated as the SSH ENSO index).

During the positive ENSO phase of the observations, shown in Fig. 2a, anomalously warm SSTs are evident in the eastern and central equatorial Pacific and are surrounded by anomalously cool SSTs in the western tropical, the North and the South Pacific. Similarly, positive ENSO modes/El Niño SST patterns can be seen in the regression maps of the simulated SSTs of the ENSO indices (Fig. 2b, c). The spectra of the simulated ENSO indices peak at 3.2, 3.6, and 4.8 years (Fig. 2e, f), which agrees well with the observed spectrum (Fig. 2d). The BCM well captures the observed seasonal cycle of ENSO (Figure S1). In general, the BCM produces relatively realistic spatial structures and spectral characteristics of ENSO (a more detailed evaluation is shown in Figures S1–S5). However, some model biases still exist. The simulated warm tongue along the equator associated with El Niño episodes is narrow and penetrates too far westward compared to that observed, which is a common problem for coupled models (Capotondi et al. 2006; Wang et al. 2012). Further, the EXT600 simulation underestimates the natural variability of SSTs in the central equatorial Pacific (Figure S2) and zonal wind anomalies during El Niño episodes (Figure S3), which is partly due to a lower level of greenhouse gases than those observed (Cai et al. 2014, 2015b). In fact, similarly weak inter-annual variations are also found in other models (e.g., Capotondi et al. 2006; Zheng 2014).

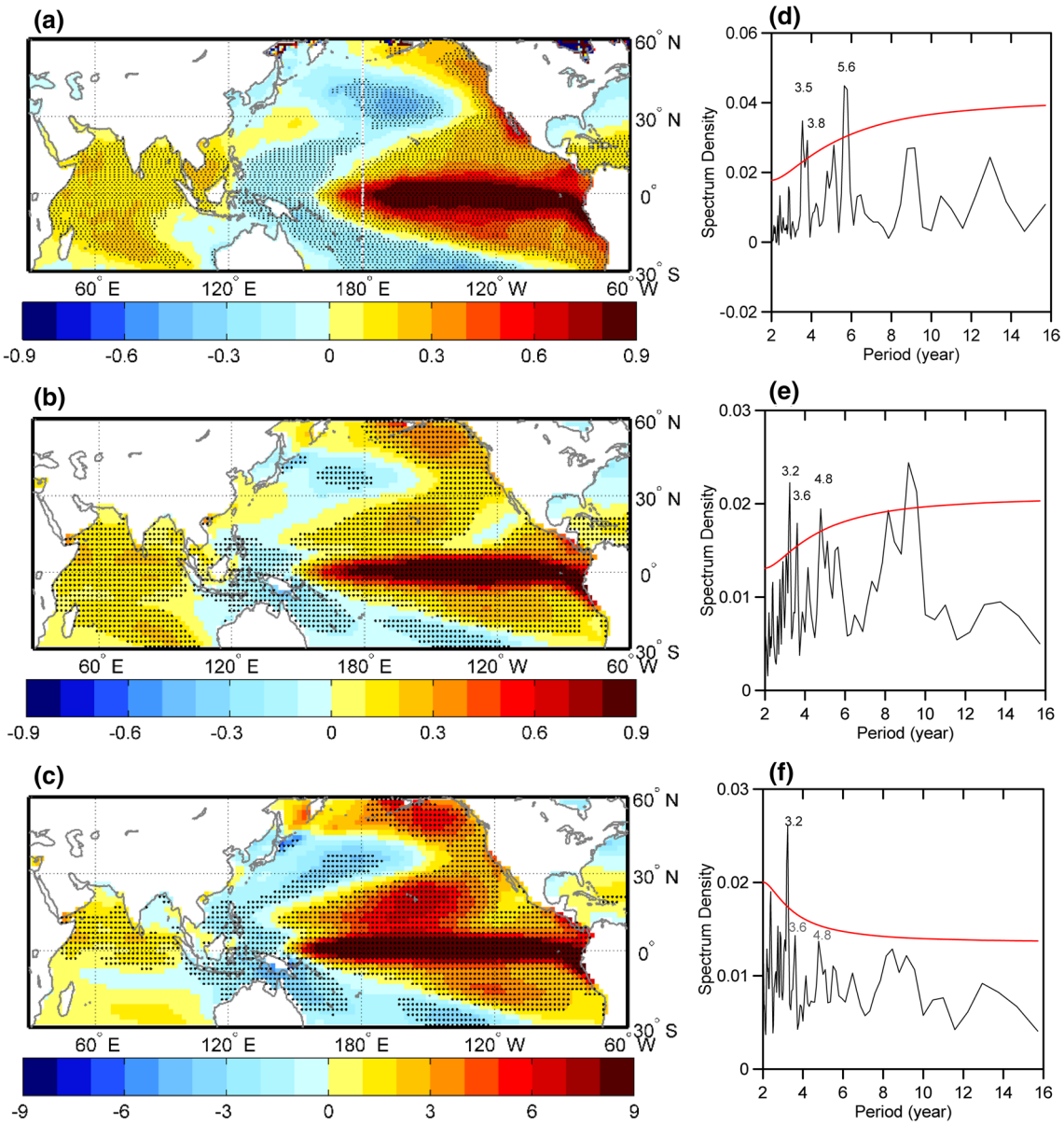

Fig. 2 **a** Regression of observed SST on the SST ENSO index (unit: °C $°C^{-1}$); Regression of simulated SST, **b** on the SST ENSO index (unit: °C $°C^{-1}$) and **c** on the SSH ENSO index (unit: °C m^{-1}) in EXT600. Areas with confidence level exceeding 99% are denoted with dots; Power spectra from annual, **d** observed SST ENSO index, **e** simulated SST ENSO index, and **f** simulated SSH ENSO index. Red curves represent 95% confidence level

3.2 Simulated ENSO evolutions following SVEs

There are eighteen SVEs in the EXT600 simulation, which are defined as the cases with anomalous peak negative global radiative forcings greater than 1 W m^{-2} (Fig. 1a and Table S1). Figure 3 illustrates the normalized SEA of the two ENSO indices for the SVE cases. The changes in the SST ENSO index (Fig. 3a) indicate that negative SSTs switch to positive SSTs during the 7th and 12th post-peak-eruption months and switch back to negative SSTs during the 18th and 31st post-peak-eruption months. The significant negative SST anomalies around the 20th post-peak-eruption month suggest a negative phase of ENSO. Similarly, the SSH ENSO index (Fig. 3b) also shows the negative-positive-negative phase trends responses to an SVE. The SSH ENSO index reaches a maximum positive value around the 7th post-peak-eruption month, corresponding to the positive SST ENSO index. Therefore, considering the changes in both ENSO indices, the simulated tropical Pacific tends to produce a negative ENSO phase after the SVEs and then

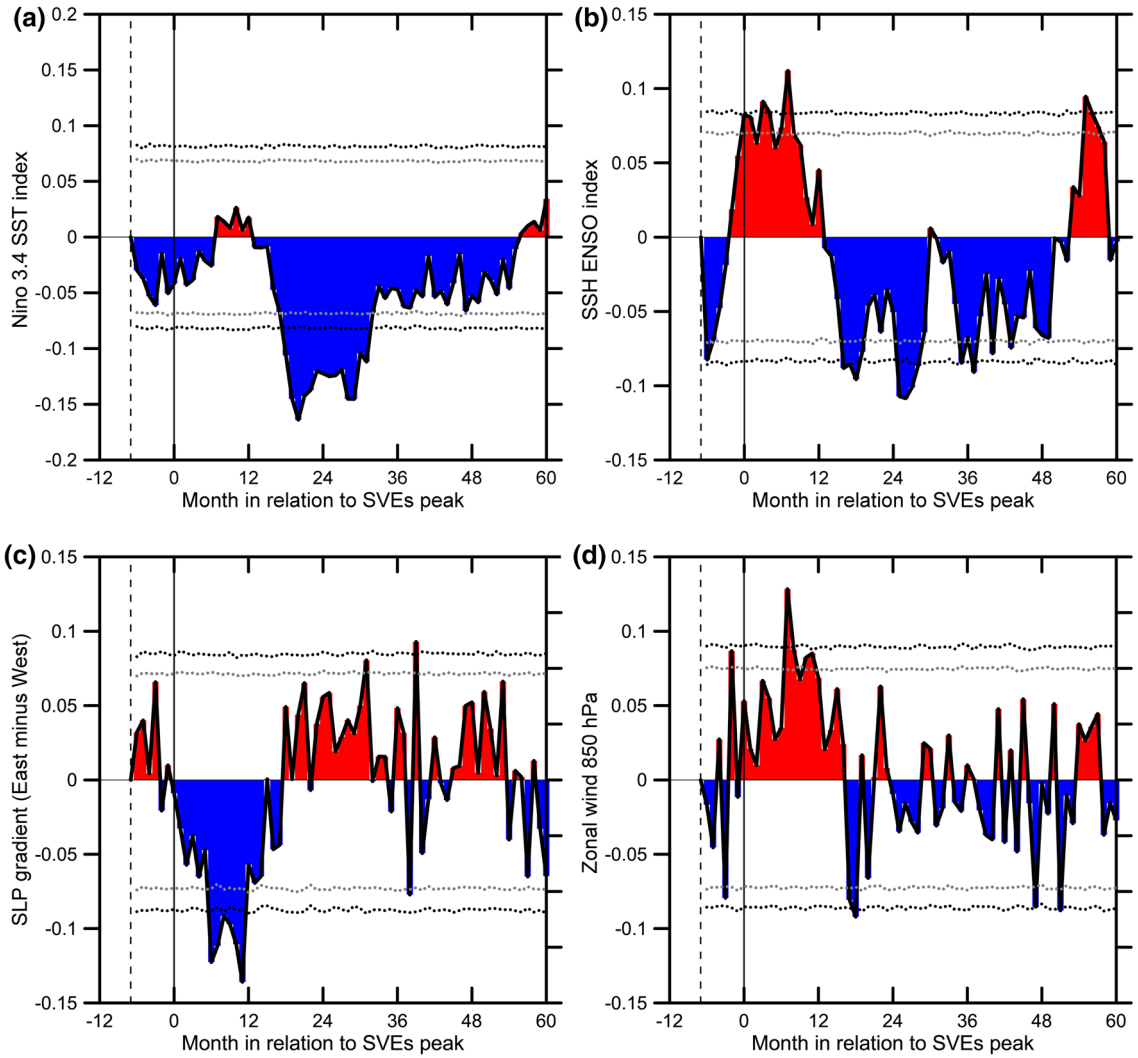

Fig. 3 Normalized SEA of simulated post-eruption evolution of four indices anomalies in the BCM EXT600 simulation: **a** the SST ENSO index, **b** the SSH ENSO index, **c** the SLP gradient over the tropical Pacific [(160°W–80°W, 5°S–5°N) minus (80°E–160°E, 5°S–5°N), (Vecchi et al. 2006)], and **d** averaged zonal wind (850 hPa) over the Niño 3.4 region. The indices anomalies are evaluated relative to 60 pre-eruption months. Solid vertical lines stand for the peak time of the SVEs, dashed vertical lines stand for the average eruption start time. Black (gray) dashed curves represent 95% (90%) confidence intervals

switches to a positive ENSO phase. Finally, the simulated tropical Pacific shifts back to a negative ENSO phase around the 20th post-peak-eruption month.

The composite averaged SST anomalies from the 24th pre-peak-eruption month to the 60th post-peak-eruption month further confirm the abovementioned responses of ENSO following SVEs (Fig. 4). After SVEs, negative SST anomalies are evident in the eastern equatorial Pacific, showing an immediate La Niña-like SST anomaly. After the peak eruption, the western equatorial Pacific is significantly cooled, and the cooling signal lasts longer than 2 years. Positive SST anomalies emerge over the central-eastern equatorial Pacific around the 6th post-peak-eruption month (Fig. 4a) and are significant in the composite SST anomaly pattern (Fig. 5a). The significant but narrow warming is evident along the central-eastern equatorial Pacific, explaining the non-significant warming in Fig. 4a. At the same time, negative SST anomalies are found over the surrounding ocean regions and are particularly strong over the western tropical Pacific. This anomalous SST pattern suggests that the tropical Pacific experiences a positive ENSO phase from the 6th to the 12th post-peak-eruption month. During this period, positive and negative SSH anomalies are observed over the central-eastern equatorial Pacific and the western tropical Pacific, respectively, and are consistent with the SST patterns during the positive phase of ENSO (Figs. 4b, 5b).

The central-eastern equatorial Pacific starts to cool in the 12th post-peak-eruption month (Fig. 4a). Significant

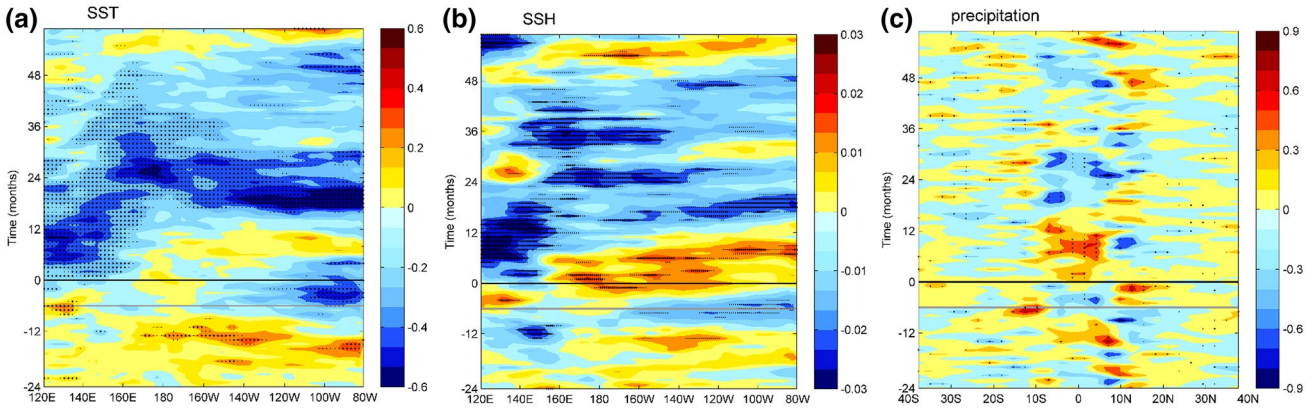

Fig. 4 Meridional averaged **a** SST anomalies (unit: °C) and **b** SSH anomalies (unit: m) over the equatorial Pacific (from 5°N to 5°S), and **c** zonal averaged precipitation anomalies (unit: mm d^{-1}) over the tropical Pacific (from 160°E to 100°W) in the BCM EXT600 simulation. The reference period is 5 years before eruption start time. The black lines stand for the peak time of the SVEs, the gray lines stand for the average eruption start time. Before analysis, the data is deseasonalized. Areas with confidence level exceeding 95% (90%) are denoted with (small) dots

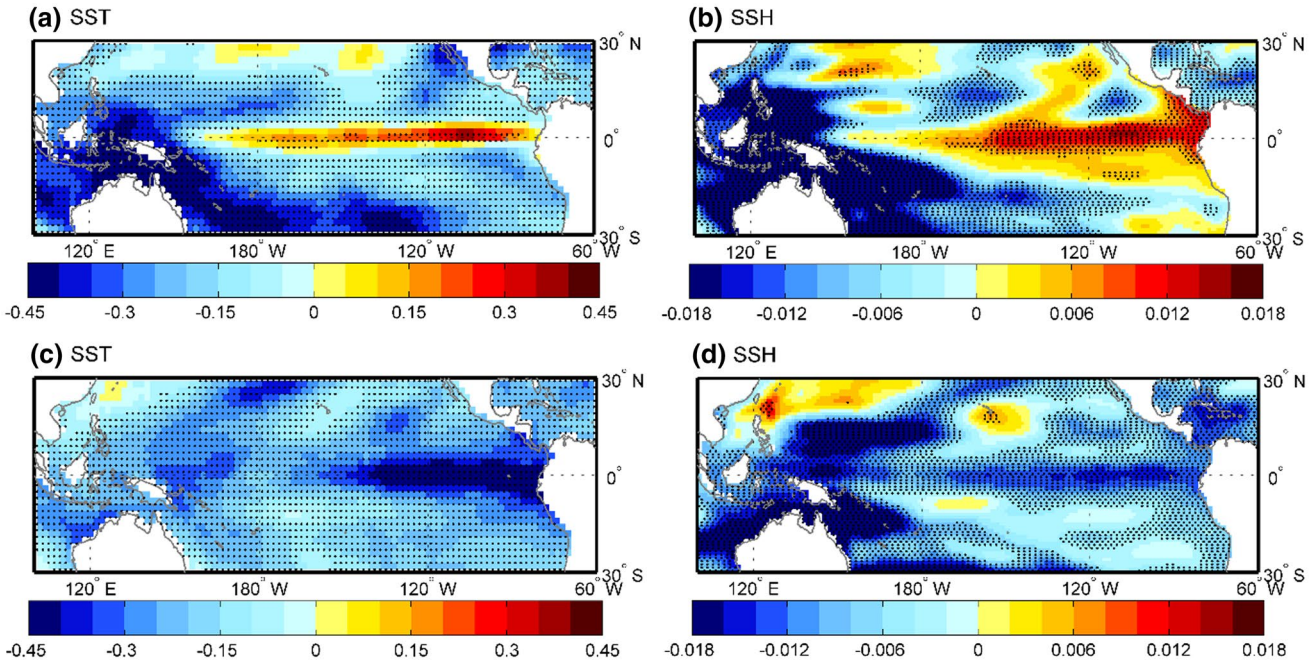

Fig. 5 SST anomalies (unit: °C) for **a** the period from the 6th to 12th post-peak-eruption months and **c** the period from the 16th to 24th post-peak-eruption months in the BCM EXT600 simulation. **b, d** are the same as **a, c**, but for SSH anomalies (unit: m). The reference period is 5 years before eruption start time. Before analysis, the data is deseasonalized. Areas with confidence level exceeding 95% are denoted with dots

negative SST anomalies are evident over the central-eastern equatorial Pacific from the 16th to the 24th post-peak-eruption months (also shown in Fig. 5c) and are much stronger than those that occurred immediately after SVEs. Correspondingly, the negative SST anomalies become weaker over the western tropical Pacific. During this period, negative SSH anomalies are found over the entire tropical Pacific (Figs. 4b, 5d) with stronger signals in the central-eastern tropical Pacific. These changes in SST and SSH anomalies indicate that the tropical Pacific enters a negative ENSO phase from the 12th to the 24th post-peak-eruption month, as indicated by the SEA of the ENSO indices.

To summarize, the composite analysis of the EXT600 suggests that, following SVEs, the eastern equatorial Pacific undergoes a brief La Niña-like cooling, an El Niño-like warming (from the 6th to the 12th post-peak-eruption

month), and finally, a longer and stronger La Niña-like cooling (from the 16th to the 24th post-peak month). Continuous responses correspond to different volcanic forcing stages from the initial step to the peak and finally decline.

3.3 Mechanism for the ENSO phase transition

To understand how SVEs affect ENSO evolution, we evaluate associated atmospheric and oceanic processes along with the ENSO transition. In particular, we analyze changes at the 20 °C isotherm depth, which describe the variations of the simulated thermocline at the equatorial Pacific (Figure S4).

Following SVEs (i.e., the initial forcing stage), significant negative SST anomalies are evident only in the eastern equatorial Pacific, showing a La Niña-like cooling (Fig. 4a). These uneven SST anomalies in the equatorial Pacific are likely caused by the quick responses of atmospheric circulations and precipitation to SVEs. After the eruption, the surface net solar radiation decreases over the tropics, which is stronger and precedes that over the midlatitudes (Figure S6). Correspondingly, the cooling in the tropical troposphere is stronger, and thus, leads to a reduced temperature gradient from the tropics to the midlatitudes at the beginning of an eruption (Figure S7). As a result, the ITCZ and South Pacific convergence zone (SPCZ) shift poleward (Figs. 4c, 6a, b) and are considerably strengthened over the western tropical Pacific. Thus, the total cloud cover decreases and offsets the SVE-induced decreases of the net surface solar radiation

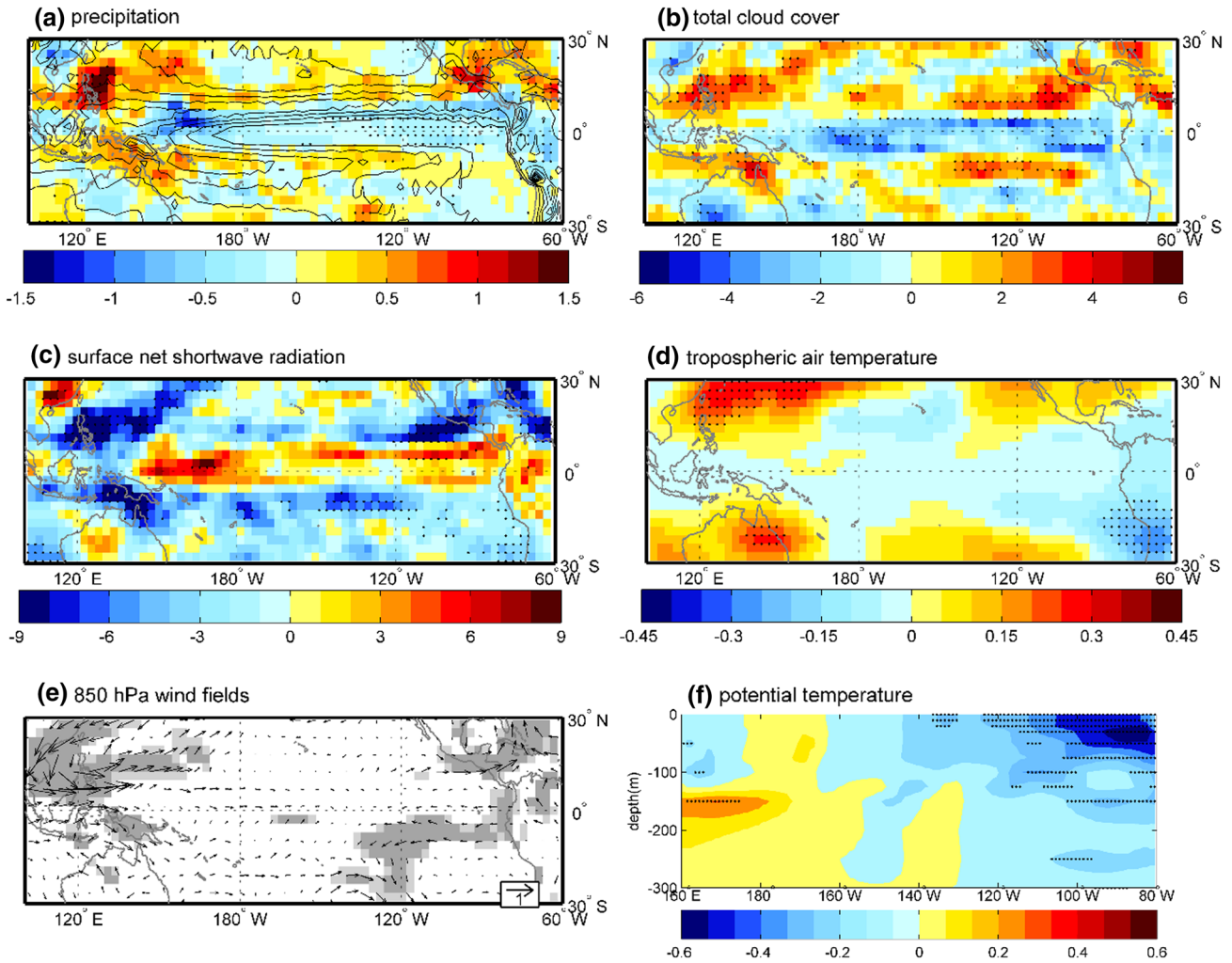

Fig. 6 Anomalous **a** precipitation (line contours indicate the climatological precipitation, unit: mm d^{-1}), **b** total cloud cover (unit: %), **c** surface net shortwave radiation (W m^{-1}), **d** averaged tropospheric air temperature (from 700 to 300 hPa, unit: °C), **e** 850 hPa wind fields (unit: m s^{-1}), and **f** potential temperature over the equatorial Pacific (from 5°N to 5°S, unit: °C) for the period from the 3th to 5th post-eruption months in the BCM EXT600 simulation. The reference period is 5 years before eruption start time. Before analysis, the data is deseasonalized. Areas with confidence level exceeding 95% are denoted with dots or shaded with gray (light gray for 90% confidence level)

along the equator at the start of the eruption. Thus, no significant surface cooling can be found in the central-western equatorial Pacific (Figure S8a). In the eastern equatorial Pacific, the SVE-induced stronger cooling along the western coast of the South American continent (Fig. 6d and S8a) results in strengthened trade winds over the eastern tropical Pacific (Fig. 6e). As a result, the thermocline is shallower in the eastern equatorial Pacific (Fig. 7a). The upwelling of the cold subsurface water is enhanced and lowers the SSTs in the eastern equatorial Pacific (Fig. 6f). Therefore, strong negative SST anomalies can be found in the eastern equatorial Pacific, showing a La Niña-like cooling following the SVEs.

At the same time, increased precipitation over the western Pacific, which is mainly caused by the poleward shifting of the ITCZ, releases more latent heat and causes anomalous tropospheric warming away from the equator (Fig. 6d). This anomalous warming pattern can lead to westerly wind anomalies (Fig. 6e) over the western equatorial Pacific through the quasi-geostrophic balance (Matsuno 1966; Gill 1980), thereby deepening the thermocline (Fig. 7a) and causing a downwelling Kelvin wave in the western equatorial Pacific (Fig. 8). Therefore, the necessary conditions for the evolution of an El Niño, as noted by Lai et al. (2015), form after SVEs. However, these westerly wind anomalies extend just to the west of the International Date Line (Figs. 6e, 7b). Thus, the downwelling Kelvin wave propagates to the central Pacific rather than reaching the eastern equatorial Pacific during this period (Figs. 7a, 8). This process is similar to the formation of central El Niño events, explaining the SST warming (non-significant) in the central equatorial Pacific during this stage (Figs. 4a, 6f).

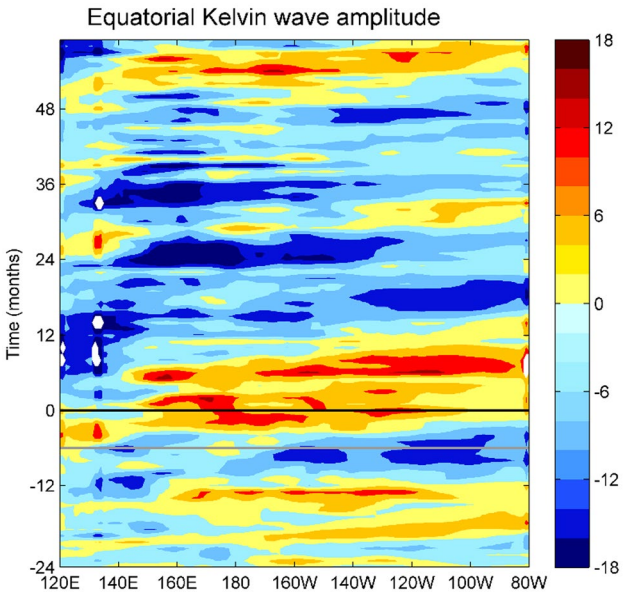

Fig. 8 Equatorial Kelvin wave amplitude anomalies (unit: cm s^{-1}) in the BCM EXT600 simulation, the reference period is 5 years before eruption start time. The black lines stand for the peak time of the SVEs, the gray lines stand for the average eruption start time. Positive (negative) values stand for down-welling (upwelling) Kelvin waves

Within 1 year after the peak time of the SVEs, the cooling effect increases at midlatitudes (Figure S6). Although the cooling effect is still weaker over the midlatitude regions than that over the tropics, stronger tropospheric cooling can be seen over the midlatitude land areas (Fig. 9a and S7b) due to smaller heat capacity of the land than the ocean

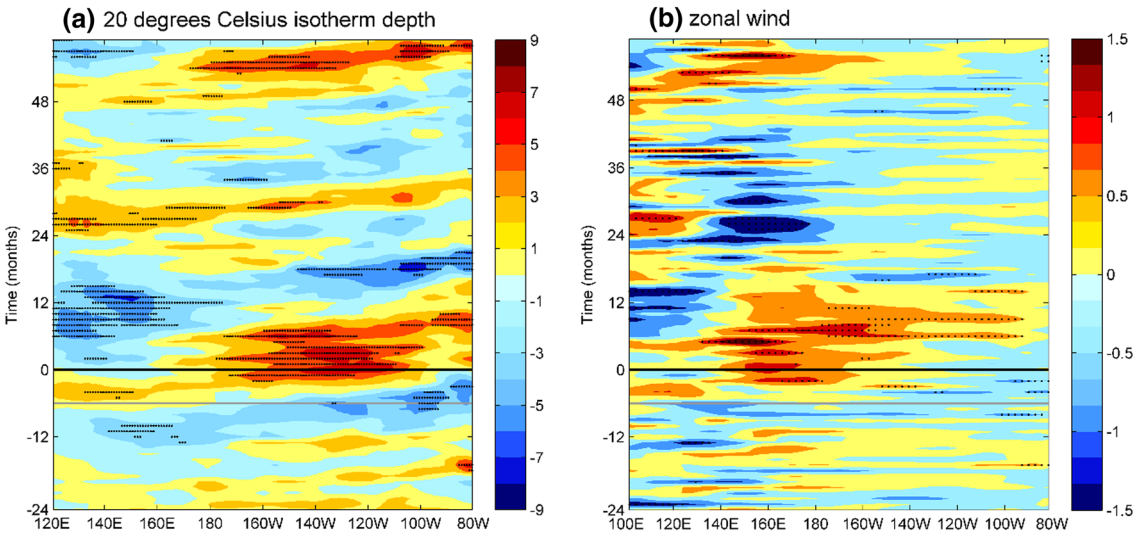

Fig. 7 Meridional averaged **a** 20 °C isotherm depth anomalies (unit: m) and **b** zonal wind anomalies (unit: m s^{-1}) at 850 hPa over the equatorial Pacific (from 5°N to 5°S) in the BCM EXT600 simulation. The reference period is 5 years before eruption start time. The black lines stand for the peak time of the SVEs, the gray lines stand for the average eruption start time. Before analysis, the data is deseasonalized. Areas with confidence level exceeding 95% are denoted with dots

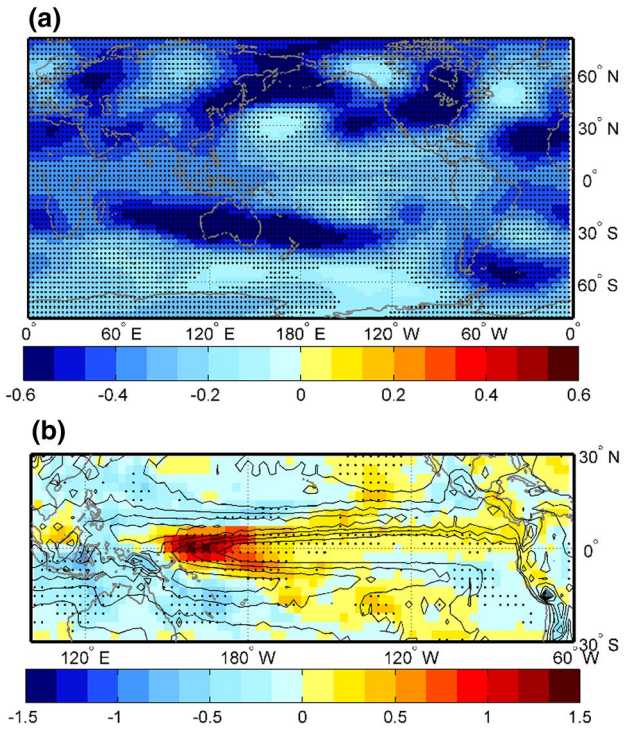

Fig. 9 Anomalous **a** averaged tropospheric air temperature (from 700 to 300 hPa, unit: °C), and **b** precipitation (line contours indicate the climatological precipitation, unit: mm d^{-1}) for the period from the peak time to 12th post-peak-eruption months in the BCM EXT600 simulation. The reference period is 5 years before eruption start time. Before analysis, the data is deseasonalized. Areas with confidence level exceeding 95% are denoted with dots

(Robock 2000; Khodri et al. 2017). Strong cooling can also be found over subtropical cloud-free ocean areas. This may be because the volcanic forcing can directly reduce surface and tropospheric air temperature and avoid the possible influences from cloud feedbacks. As a result, the temperature gradient increases from the equator to the midlatitudes. Thus, the ITCZ and SPCZ weaken and shift toward the equator (Figs. 4c, 9b), contributing to the weakening of the trade winds in the central equatorial Pacific (Fig. 7b). A similar process is found in the recently completed Community Earth System Model (CESM) Last Millennium Ensemble (LME) simulation (Stevenson et al. 2016; Liu et al. 2017). The mentioned uneven SST anomalies shift the convective activity from the western equatorial Pacific eastwards (Fig. 9b and S9) and further enhance the westerly wind anomalies over the western Pacific (Fig. 7b), as documented by Graf (1986). Additionally, the equatorward-shifted and weakened ITCZ and SPCZ as well as the eastward tropical convective activity weakens the sea level pressure (SLP) over the tropical Pacific during this period (Fig. 10a).

At the same time, a stronger surface cooling is evident over the Maritime Continent region (Fig. 10b) due to the dynamical thermostat mechanism (Emile-Geay et al. 2008) and the smaller heat capacity of the land. As a result, the SLP over the Maritime Continent increases significantly (Fig. 10a), which plays an important role in weakening the east–west SLP gradient over the tropical Pacific (Fig. 3c). Therefore, the westerly wind anomalies are further strengthened (Fig. 3d) and extend into the eastern tropical Pacific

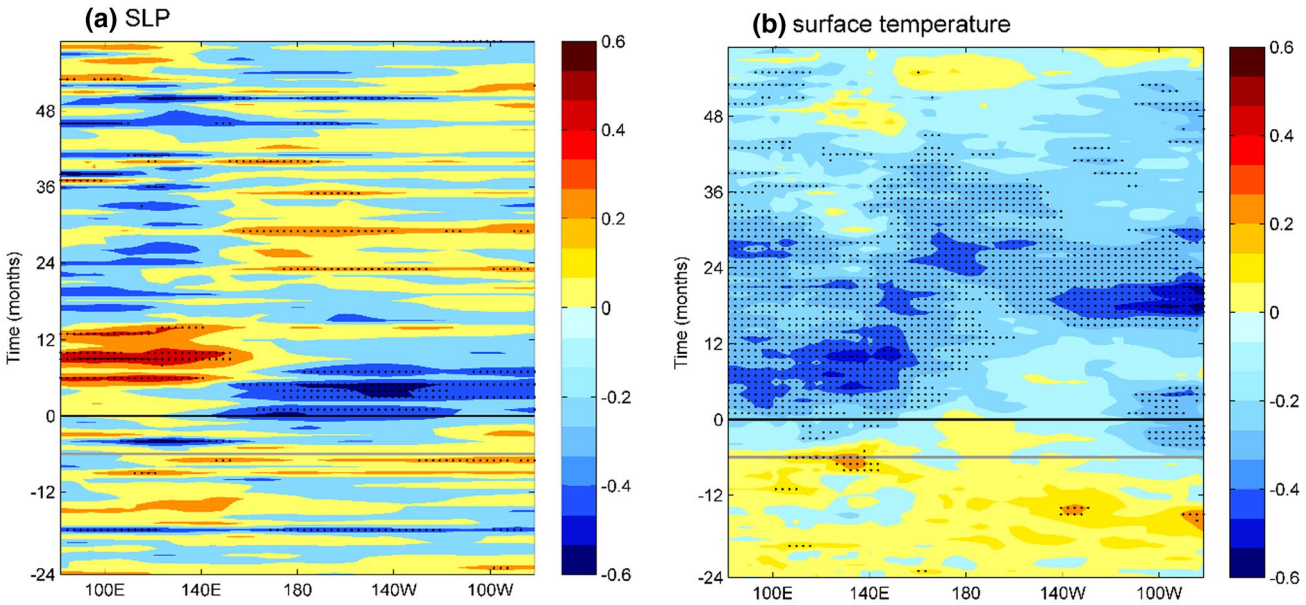

Fig. 10 Meridional averaged **a** SLP anomalies (unit: hPa) and **b** surface temperature anomalies (unit: °C) over the tropical Pacific (from 15°N to 15°S) in the BCM EXT600 simulation, the reference period is 5 years before eruption start time. The black lines stand for the peak time of the SVEs, the gray lines stand for the average eruption start time. Before analysis, the data is deseasonalized. Areas with confidence level exceeding 95% are denoted with dots

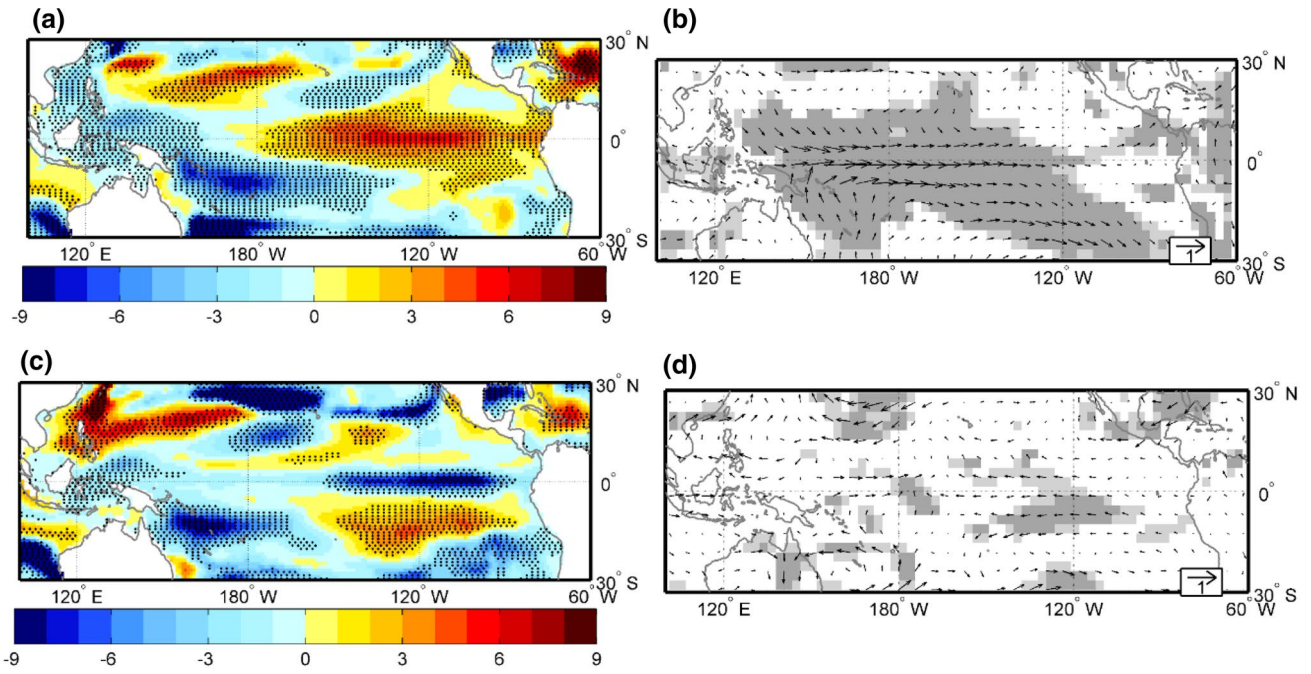

Fig. 11 The 20 °C isotherm depth anomalies (unit: m) for **a** the period from the peak time to 12th post-peak-eruption months and **c** the period from the 16th to 20th post-peak months in the BCM EXT600 simulation. Areas with confidence level exceeding 95% are denoted with dots. **b, d** are the same as **a, c**, but for wind anomalies at 850 hPa (unit: m s^{-1}). Areas with confidence level exceeding 95% (90%) are shaded with (light) gray. The reference period is 5 years before eruption start time. Before analysis, the data is deseasonalized

from the 6th post-peak-eruption month (Figs. 7b, 11b). Finally, these wind anomalies excite an El Niño-like response through the Bjerknes feedback during the period from the 6th to 12th post-peak-eruption months (Fig. 5a, b). At the same time, significant easterly wind anomalies emerge over the western tropical Pacific from the 6th post-peak-eruption month (Fig. 7b). As a result, the thermocline becomes shallower in the western tropical Pacific (Fig. 7a) and an upwelling Kelvin wave is excited (Fig. 8), suggesting that the western Pacific has a discharged thermocline state in terms of the recharge-discharge oscillator (Jin 1997a, b) at the onset of an SVE-induced El Niño-like response.

In the BCM EXT600 simulation, both the weakened, equatorward-shifted convergence zones and stronger cooling over the Maritime Continent contribute to the westerly wind anomalies, which are the key drivers of an El Niño-like response in the peak forcing stage. To examine the relative importance of these two factors, we carried out a set of AGCM experiments using CAM4. The simulation with default configuration "F_2000" is used as the control simulation. The atmospheric composition was constant in the year 2000. A prescribed climatology for SST and sea ice is provided for current climate simulations by NCAR. In the first sensitivity simulation (hereafter called CAM4_GSSTA), the averaged global SST anomalies from the 6th to 8th post-peak-eruption months are added into the CAM4 SST climatology. This time period was selected because of when the westerly wind anomalies begin extending to the eastern equatorial Pacific. In addition, another two sensitivity simulations using CAM4 are designed. One is named CAM4_MCSSTA, in which only SST anomalies around the Maritime Continent (20°S–15°N and 90°–160°E) are added to the CAM4 SST climatology. In contrast, in the other sensitivity simulation (hereafter called CAM4_NoMCSSTA), SST anomalies are imposed in the whole domain except for regions around the Maritime Continent, where CAM4 SST climatology are imposed. All the CAM4 simulations are consecutively integrated for 40 years, and the final 30 years are analyzed below.

Forced by global anomalous SSTs (i.e., CAM4_GSSTA), CAM4 simulates increased SLP anomalies over the western tropical Pacific, particularly over the Maritime Continent, whereas the decreased SLP anomalies over the central-eastern tropical Pacific (Fig. 12b). At the same time, precipitation increases significantly along the whole equatorial Pacific and is reduced over the surrounding region and Maritime Continent (Fig. 13b). The simulated SLPs and precipitation anomaly patterns strongly resemble those in the BCM EXT600 simulation (Figs. 12a, 13a), indicating a reduced east–west SLP gradient and weakened, equatorward shift of the ITCZ and SPCZ. The associated westerly wind anomalies are also evident over the whole equatorial Pacific in the CAM4_GSSTA simulation. In addition, equatorial easterly wind anomalies can be found west of 120°E, implying a

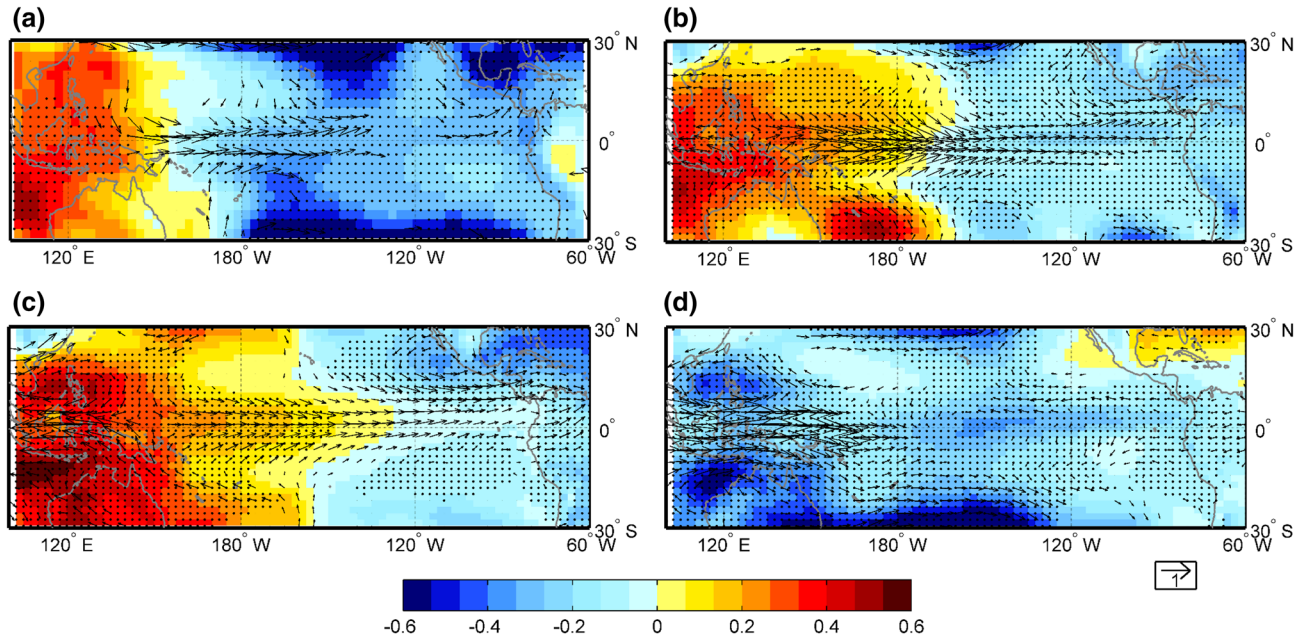

Fig. 12 **a** SLP (unit: hPa) and 850 hPa wind fields (unit: m s^{-1}) anomalies for the period from the 6th to 8th post-peak-eruption months in the BCM EXT600 simulation. Differences in SLP and 850 hPa wind fields between **b** CAM4_GSSTA, **c** CAM4_MCSSTA, **d** CAM4_NoMCSSTA and control simulation (sensitivity simulation minus control simulation). Areas with confidence level exceeding 95% are denoted with dots. For the 850 hPa wind fields, only areas with confidence level exceeding 95% are shown in the figure

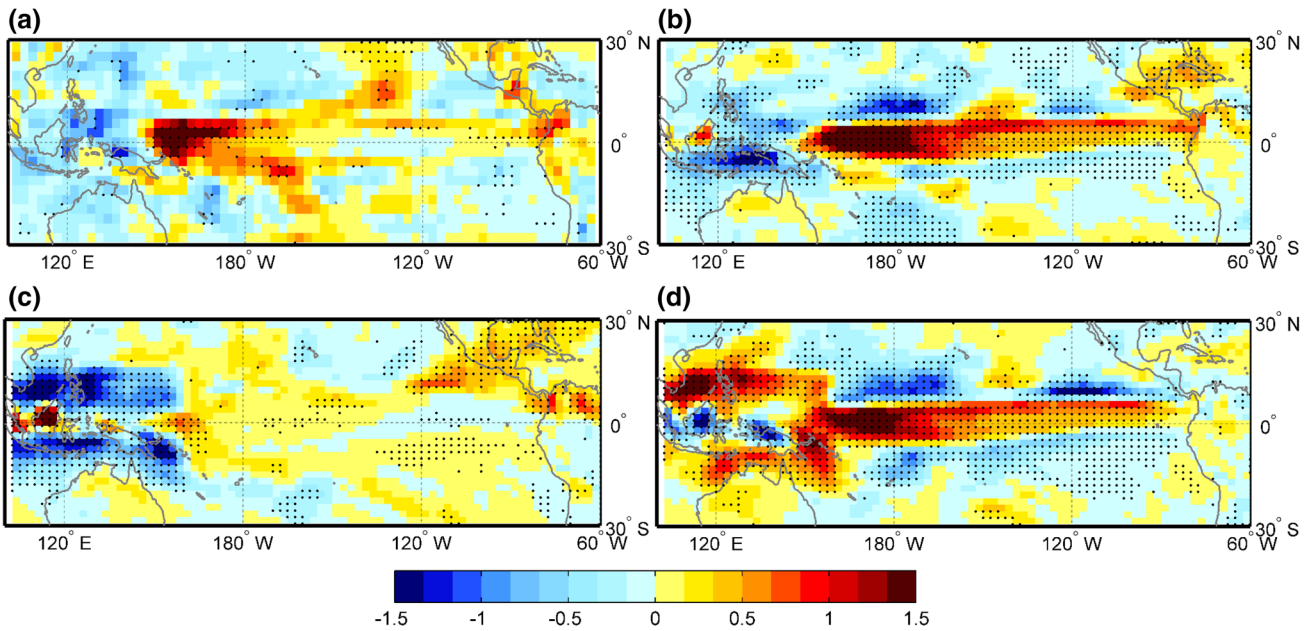

Fig. 13 **a** Precipitation anomalies (unit: mm d^{-1}) for the period from the 6th to 8th post-peak-eruption months in the BCM EXT600 simulation. Differences in precipitation between **b** CAM4_GSSTA, **c** CAM4_MCSSTA, **d** CAM4_NoMCSSTA and control simulation (sensitivity simulation minus control simulation). Areas with confidence level exceeding 95% are denoted with dots

suppressed convection and an anomalous divergence of the lower troposphere over the Maritime Continent.

Similar changes in SLPs and the lower tropospheric circulation can be found in the CAM4_MCSSTA simulation (Fig. 12c), suggesting the important role of cooling around the Maritime Continent in causing westerly wind anomalies from west to east over the whole equatorial Pacific. Compared with the results from CAM4_GSSTA, the westerly

wind anomalies are stronger and the positive SLP anomalies over western tropical Pacific extend farther east. These stronger responses of the atmosphere to the cooling around the Maritime Continent are mainly due to the absence of cooling over other Pacific regions. For this reason, changes in ITCZ and SPCZ as well as the related precipitation anomalies are not implemented in this simulation (Fig. 13c).

Conversely, westerly wind anomalies are evident only over the Maritime Continent and the equatorial western Pacific regions, rather than extending to the equatorial eastern Pacific in the CAM4_NoMCSSTA simulation (Fig. 12d), suggesting that the weakened and equatorward shifts of the tropical convergence zones (Fig. 13d) can lead to westerly wind anomalies over only the tropical western Pacific. Based on this kind of designed CAM4 simulations and similarities of CAM4 and BCM results, both the weakened and equatorward-shifted ITCZ and SPCZ as well as the stronger cooling over the Maritime Continent can contribute to the formation of westerly wind anomalies over the equatorial Pacific during the peak forcing stage. Further, the latter factor is suggested to be more important for extending the westerly wind anomalies to the equatorial eastern Pacific, and thereby exciting an El Niño-like response. In addition, easterly wind anomalies over the tropical western Pacific are also absent in the CAM4_NoMCSSTA simulation. It suggests that the stronger cooling suppressing convection over the Maritime Continent is probably the main reason for the easterly wind anomalies over the tropical western Pacific during the peak forcing stage.

As the volcanic forcing weakens (i.e., in the declining forcing stage), the cooling around the Maritime Continent weakens and becomes comparable to that over the central equatorial Pacific (Fig. 10b). Therefore, the east–west SLP gradient (Figs. 3c, 10a) and the trade winds (Figs. 3d, 11d) recover starting in the 13th post-peak-eruption month. As a result, the upwelling Kelvin wave begins to propagate eastward (Fig. 8). The equatorial Pacific starts transitioning to a negative ENSO phase after the SVE-induced El Niño-like response, which is similar to the observed phase transition of ENSO (McPhaden and Yu 1999; Picaut et al. 2002; Zheng and Zhu 2015) and that of another coupled model (Kug et al. 2006). When the upwelling Kelvin wave reaches the eastern equatorial Pacific (Fig. 8), the thermocline becomes shallow and thereby enhances the upwelling of the subsurface waters in the eastern equatorial Pacific (Figs. 7a, 11c). Therefore, through the Bjerknes feedback, negative SST and SSH anomalies occur in the eastern tropical Pacific (Figs. 4a, b, 5c, d). The tropical Pacific eventually enters a negative ENSO phase, showing a strong La Niña-like response.

In fact, the upper-ocean heat contents in the tropical western Pacific and that of the off-equatorial central-eastern Pacific have been significantly reduced by SVE-induced large-scale cooling forcing from the peak forcing stage (Fig. 5b, d). On the one hand, this forcing directly cools the tropical Pacific SST, partly explaining the reason for a narrower and weaker El Niño-like warming in the second stage, relative to normal El Niño events. On the other hand, this forcing further enhances the negative thermocline anomalies and causes a stronger discharged thermocline state in the western equatorial Pacific in the following months (Fig. 7a), contributing to the formation of a stronger and longer-term La Niña response in the declining forcing stage. Therefore, the persistent cooling effect due to the eruption weakens the El Niño-like response during the peak forcing stage (Figs. 3a, 4a, 5a) but strengthens the La Niña-like response in the declining forcing stage (Figs. 3a, 4a, 5c).

4 Observed ENSO evolution and SVEs

4.1 Recent observations and simulations

There were three SVEs during the period of 1948–2008: the Mount Agung eruption in 1963, the El Chichón eruption in 1982, and the Mount Pinatubo eruption in 1991. During the post-eruption winters, significant positive SST anomalies are observed over the central-eastern tropical Pacific (Graf et al. 2014), suggesting the co-occurrence of positive ENSO phases and SVEs. As indicated by the SST ENSO indices in Fig. 14, El Niño events rapidly developed in the tropical Pacific following these three SVEs. These El Niño events all reached their peak phases in the post-peak-eruption month and then begin to decay. Closely following the El Niño events in 1963/1964 and 1982/1983, La Niña events formed and remained present for more than 1 year. However, the El Niño event in 1991/1992 was different. There was no significant La Niña event after the Mount Pinatubo eruption. In addition, the simulated initial and brief La Niña-like responses were also absent for these three SVEs. In general, the observed developments and transitions of ENSO phases are consistent with the simulated El Niño-like and subsequent La Niña-like responses in the BCM EXT600 simulation. Due to the absence of simulated initial and short La Niño-like responses, the onsets of the observed positive ENSO episodes are earlier and evolve faster than those in the EXT600 simulations.

Forced by the transient heat, freshwater and momentum fluxes from the NCEP/NCAR datasets, MICOM60 can well reproduce the evolution of the SST ENSO index before and after these three SVEs. In addition, the observed low-level wind anomalies over the tropical Pacific characterize similar evolutions of the ENSO index during these periods (Fig. 14), suggesting that anomalous

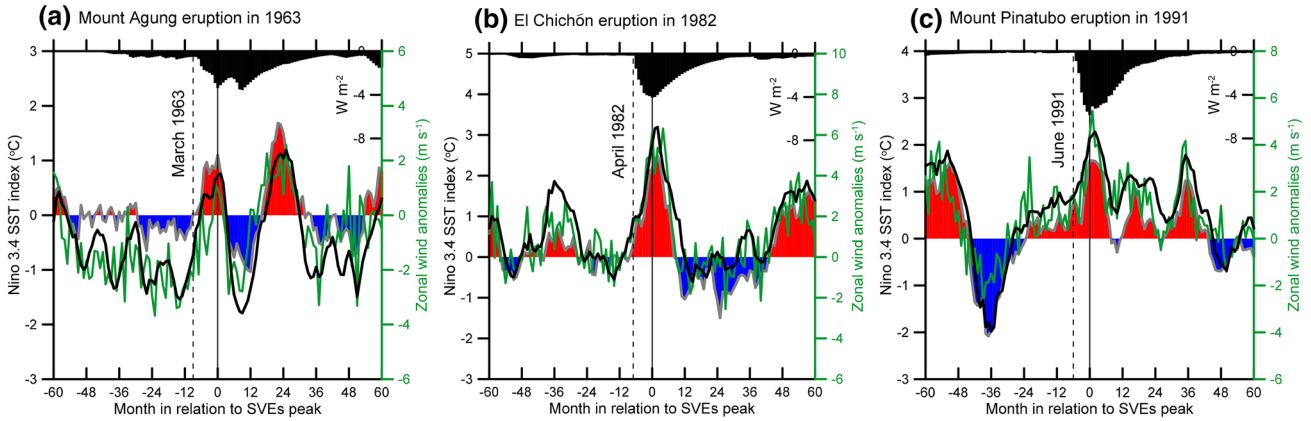

Fig. 14 Observed (shaded) and MICOM60 simulated (black curves) Niño 3.4 SST indices (unit: °C) for **a** the Mount Agung eruption, **b** the El Chichón eruption, and **c** the Mount Pinatubo eruption, respectively. Black shaded stands for the averaged tropical volcanic forcing (unit: W m^{-2}). Green curves stand for the NCEP/NCAR zonal wind anomalies at 850 hPa (unit: m s^{-1})

winds could also play an important role in the observed ENSO evolutions following SVEs.

4.2 Ocean model simulations

To investigate the roles of surface winds, heat fluxes, and freshwater fluxes in the observed evolution of ENSO after SVEs, we perform an additional four sets of numerical experiments using MICOM. Each set includes three simulations of the most recent three SVEs. These sensitive simulations cover the year before the SVE and the subsequent 10 years. Their initial states (i.e., the 1st of January in 1962, 1981, and 1990) are derived from the MICOM60 simulation. In the first set of sensitivity simulations (hereafter abbreviated as SEN1-1963, SEN1-1982, and SEN1-1991), only the daily net surface downward fluxes of solar radiation and net longwave radiations are set using the values from the year before the SVE (i.e., 1962, 1981, and 1990) for the whole simulation. It means that SVE-induced direct radiative forcing is excluded in these simulations. Other fluxes are set to follow those of the actual years. In the second set of sensitivity simulations (SEN2), only the daily net surface fluxes of sensible heat and latent heat as well as the daily precipitation rates at the surface are set equal to the values of the year before the SVE throughout. In the third set of the sensitivity simulations (SEN3), only the daily surface momentum fluxes of the zonal and meridional components are set to those of the year before the SVE. In the last set (SEN4), all the surface fluxes mentioned above are set to those of the year before the SVE for the whole simulation. The comparisons between different sets of simulations highlight the impacts of different fluxes on the ENSO evolutions following SVEs.

As shown in Fig. 15, SEN1 and SEN2 both well capture the ENSO evolutions during these three SVEs. Their results are consistent with those of the MICOM60 simulation. In contrast, SEN3, in which the anomalous surface momentum fluxes after the eruption are absent, fails to reproduce the observed changes in the SST ENSO index. This result indicates the key role of anomalous trade winds in the ENSO evolutions after SVEs. Nevertheless, compared to those of SEN4, the changes of the SST ENSO index in SEN3 are more like those of the MICOM60 simulation, suggesting that the anomalous heat and freshwater fluxes after the SVEs also, to some extent, contribute to ENSO evolution during these periods. Therefore, changes in the trade winds play the dominant role in regulating ENSO during the post-eruption period.

Note that the observed SVEs are too few to allow for conclusive causality between the SVEs and the trade winds anomalies after the eruptions. However, the EXT600 simulation proves a close link between these systems (Figs. 3d, 7b), meaning that the SVEs of the recent decades could contribute to the anomalous westerly winds and the observed El Niño events following SVEs.

5 Discussion and conclusions

We used the outputs from BCM, CAM4 and MICOM as well as observational data to investigate the influence of SVEs on ENSO evolution. We find that the BCM simulation indicates a negative-positive-negative ENSO evolution in response to SVEs, corresponding to the initial forcing stage (i.e., from the eruption to the peak forcing), the peak forcing stage (i.e., from the peak forcing to the 1 year later), and the declining forcing stage (i.e., the following year).

In the initial forcing stage, SVEs can induce stronger cooling along the western coast of the South American continent and also cause strengthened trade winds over the

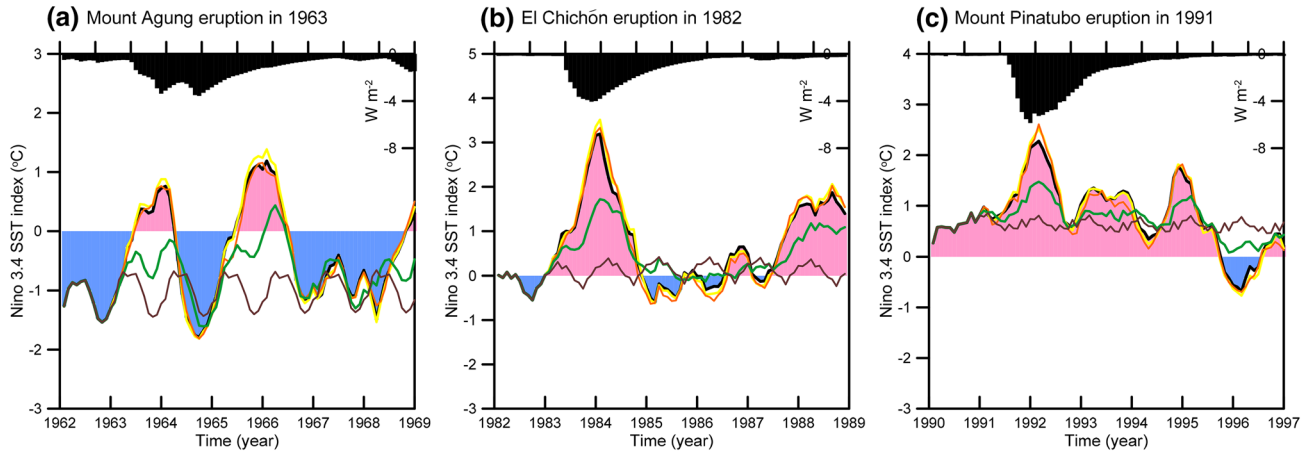

Fig. 15 Simulated Niño 3.4 SST indices (unit: °C) for **a** the Mount Agung eruption, **b** the El Chichón eruption, and **c** the Mount Pinatubo eruption, respectively. Color shading and black curves stand for the MICOM60 simulation. Black shaded stands for the averaged tropical volcanic forcing (unit: W m^{-2}). Color curves stand for the MICOM sensitivity simulations (yellow is for SEN1, orange is for SEN2, green is for SEN3, and brown is for SEN4). The seasonal cycle in the MICOM60 is removed from all sensitivity simulations

eastern tropical Pacific. Through the Bjerknes feedback, an immediate La Niña-like cooling forms in the eastern equatorial Pacific. In the peak forcing stage volcanic forcing leads to stronger surface cooling over the midlatitudes and the Maritime Continent than that over the tropical Pacific. The resulting enhanced temperature gradient from the equator to the midlatitudes together with the surface cooling over the tropical Pacific leads to a weakened and equatorward-shifted ITCZ and SPCZ. The stronger cooling over the Maritime Continent results in a reduced east–west SLP gradient. These changes cause significant westerly wind anomalies over the central-eastern tropical Pacific and thereby excite an El Niño-like response during this stage. In this stage, SVE-induced large-scale cooling over the tropics and their associated easterly wind anomalies over the western tropical Pacific promote a discharged thermocline state in the western Pacific, which favors a phase transition to La Niña or a negative ENSO. In this process, additional CAM4 simulations suggest a more important role of stronger surface cooling over the Maritime Continent in extending the westerly wind anomalies to the equatorial eastern Pacific and in shaping easterly wind anomalies over the equatorial western Pacific. During its final stage, volcanic forcing becomes too weak to maintain the westerly wind anomalies over the central-eastern tropical Pacific. As a result of the discharged thermocline state in the western Pacific and the recovering trade winds, the tropical Pacific eventually enters a negative ENSO phase. Throughout this process, the cooling effect from eruptions weakens the SVE-induced tendency for El Niño-like SST anomalies, whereas the cooling effect favors a subsequent negative ENSO phase.

Focusing on the observed three SVEs, the results from MICOM simulations also suggest the dominant role of anomalous trade winds in regulating ENSO evolution after eruptions, while heat fluxes and freshwater fluxes play secondary roles. This result is consistent with the BCM EXT600 simulation. Overall, our analysis reveals the mechanisms that allow SVEs to influence ENSO evolution, indicating that SVEs play an important role in modulating ENSO evolution.

Recently, some modeling studies focus on the cause/effect relationship between SVEs and El Niño-like responses as well as underlying mechanisms. Some of them suggest that westerly wind anomalies over the tropical Pacific play an important role in exciting El Niño-like responses during the strong volcanic eruption period. However, different causes of the emergence of westerly wind anomalies are proposed based on different coupled models' results. Cooling over the Maritime Continent (Ohba et al. 2013), equatorward-shifting of the ITCZ (e.g., Pausata et al. 2015; Lim et al. 2016; Liu et al. 2017), and enhancement of precipitation over the subtropical Pacific (Liu et al. 2017) are suggested to lead to the formation of the westerly wind anomalies. In this study, the BCM and additional CAM4 simulations emphasize a dominant role of cooling over and around the Maritime Continent in causing westerly wind anomalies, particularly for that over the equatorial eastern Pacific. At the same time, the equatorward-shifted ITCZ and SPCZ can contribute to the intensity of the westerly wind anomalies over the equatorial western-central Pacific, rather than over the whole equatorial Pacific.

Focusing on the 1991 Pinatubo eruption, a latest modeling study suggests that volcanically induced cooling in tropical Africa weakens the west African monsoon (Khodri et al. 2017). The resulting atmospheric Kelvin wave can drive equatorial westerly wind anomalies over the western

Pacific. Through air-sea interactions in the Pacific, these westerly wind anomalies are further amplified, and favour an El Niño-like response. A remote effect from tropical African cooling on weakening the Walker circulation is suggested. Different from the above study, our model results emphasize the importance of SVE-induced local surface cooling on weakening the atmospheric circulation over the tropical Pacific. Whether surface cooling over other tropical regions can contribute to the key westerly wind anomalies in the BCM and other coupled models needs further investigation.

In model–data comparisons, the BCM simulated El Niño-like warmings and subsequent La Niña-like coolings match the reconstructed ENSO responses to volcanism in most of the proxy data (Adams et al. 2003; Liu et al. 2017), specifically for the observed Mount Agung eruption in 1963 and El Chichón eruption in 1982. Conversely, the simulated initial brief La Niña-like cooling in the BCM EXT600 simulation is seen in only one ENSO reconstruction (Li et al. 2013), in which more information from adequate tropical records is included. One possible explanation for this lack of the initial La Niña-like response is that the cooling of eastern equatorial Pacific is so brief and weak that its impacts and signal are not fully recorded by most proxy data around the world. In addition, the absence of this SVE-induced initial La Niña-like cooling in the observations is probably because the responses of ENSO to eruptions are very sensitive to the initial state of the tropical Pacific (Pausata et al. 2016). After all, there have been only three SVEs over the past 60 years, and only two SVEs since the advent of the satellite era. Of course, another possibility of the formation of this initial La Niña-like response also exists: the phenomenon is probably caused by model bias due to too strong radiative cooling by volcanic forcing. Thus, accurately expressing volcanic forcing in the model is also a key issue for further volcano-related studies.

In fact, a similar initial La Niña-like cooling can also be seen in the CMIP5 multi-model results (e.g., Fig. 3a in Maher et al. 2015) and the CESM LME simulations (Fig. 6 in Liu et al. 2017). Based on later simulations, Stevenson et al. (2017) suggested that this initial cooling is mainly caused by volcanic cooling effects rather than the advective signature associated with La Niña, which differs from the BCM EXT600 simulation. Significant negative SSH and thermocline depth anomalies are evident after the eruptions (Figs. 4b, 6f, 7a), suggesting a La Niña-related dynamical

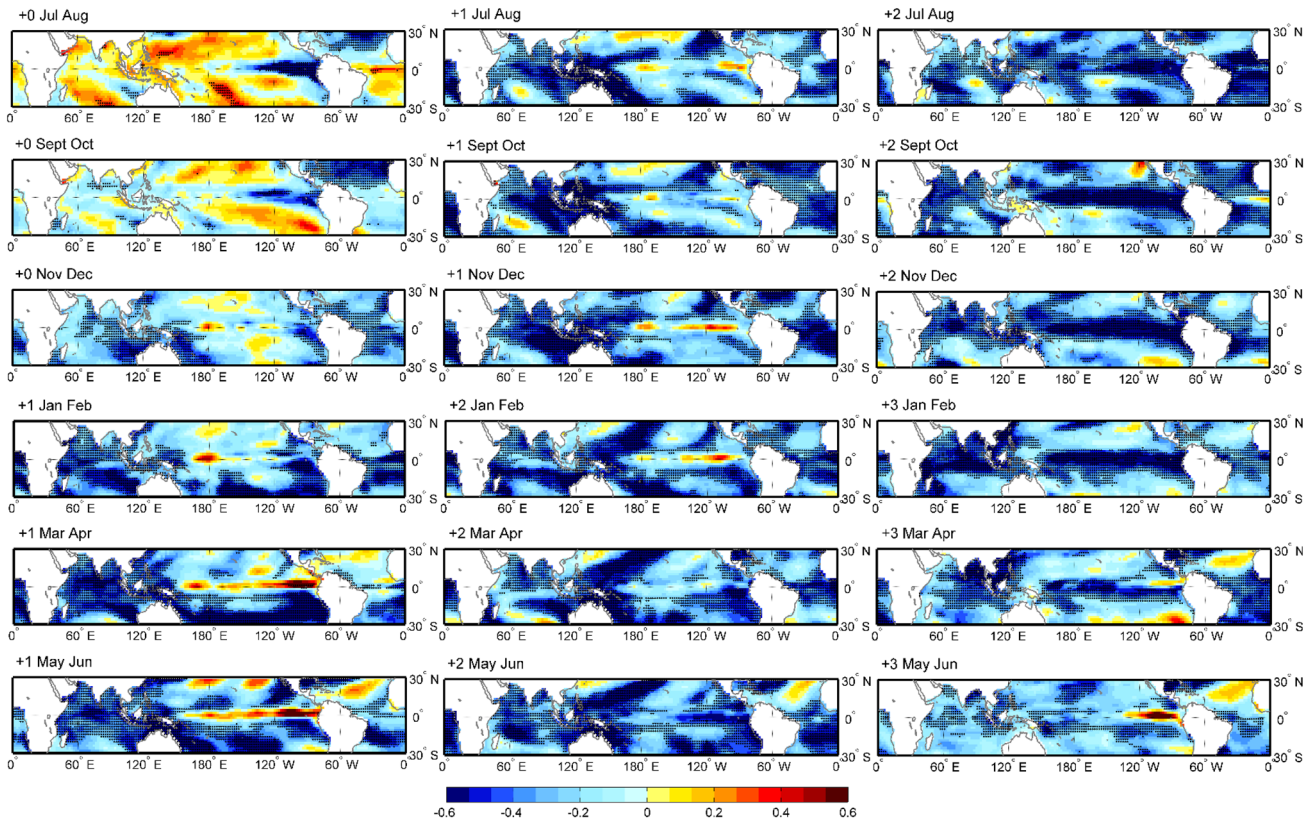

Fig. 16 Evolution of the SST anomalies in the BCM EXT600 simulation (unit: °C) from the eruption year to the third post-eruption year. The reference period is 5 years before the eruption. "0" stands for the eruption year, "+1" stands for the first post-eruption year. Areas with confidence level exceeding 95% are denoted with dots

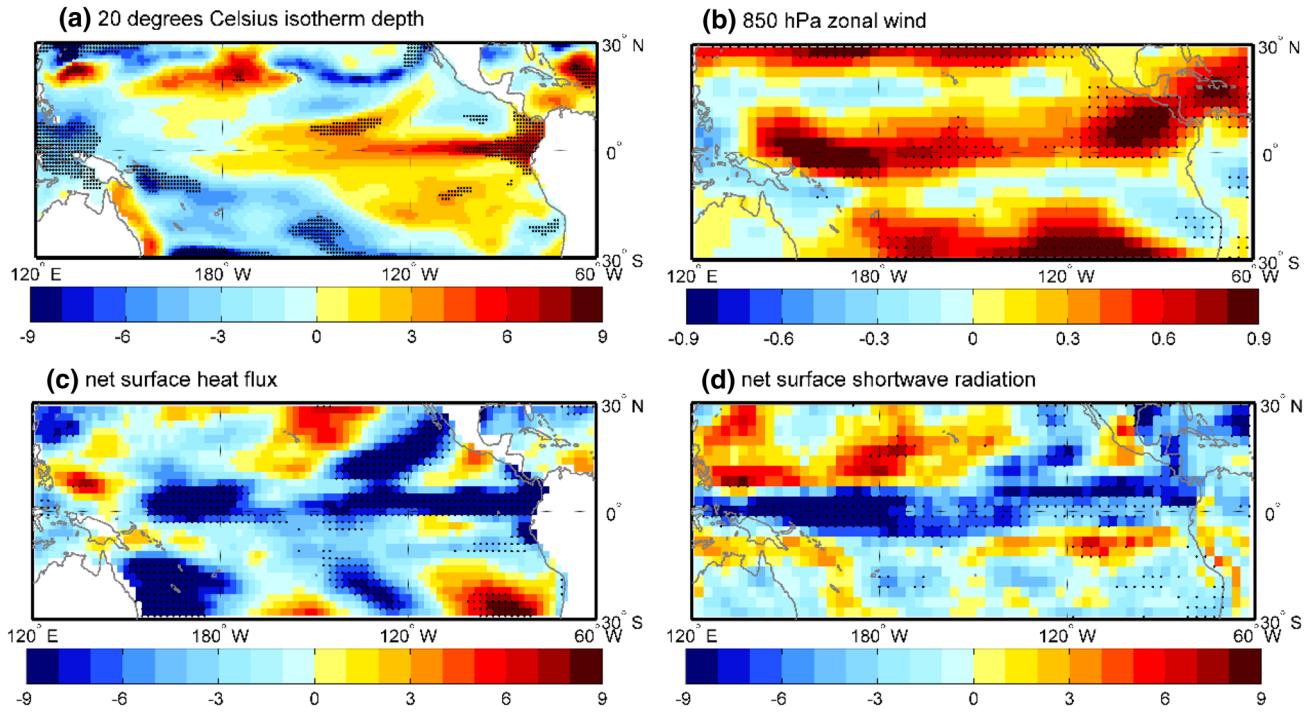

Fig. 17 Anomalous **a** 20 °C isotherm depth (unit: m), **b** 850 hPa zonal wind (unit: m s^{-1}), **c** net surface heat flux received by ocean (unit: W m^{-1}), **d** net surface shortwave radiation (unit: W m^{-1}) in the March–June of the first post-eruption year in the BCM EXT600 simulations. The reference period is 5 years before eruption start time. Areas with confidence level exceeding 95% are denoted with dots

process is included in the formation of this initial La Niña-like cooling in the BCM.

In the CESM LME simulations, the default starting month of the eruptions is April (Stevenson et al. 2017). Based on a composite analysis of each calendar month, Liu et al. (2017) indicated the transition from SVE-induced El Niño events to La Niña events is much faster than that of the unforced El Niño in the CESM LME simulations. They suggested the importance of the earlier emergence of easterly wind anomalies in January during the SVE-induced El Niño episode (which usually occurs in May for unforced El Niño events). In the BCM EXT600 simulation and most of the CMIP5 simulations (Maher et al. 2015), the start times of the SVEs are different and a deseasonalized analysis set according to the peak month is used. Based on the BCM result, the transition from an SVE-induced El Niño to La Niña coincides with the recovery of the trade winds (Fig. 3b, d). However, the final La Niña-like response is stronger and lasts longer. The volcanic cooling effect of the peak forcing stage contributes to the enhancement of the discharged thermocline state in the western Pacific, which partly explains the subsequent stronger and longer La Niña-like response.

Usually, ENSO is phase-locked, and its peak always occurs in the boreal winter. To investigate the impacts of SVEs on ENSO, in this study, we remove the seasonal cycles from the post-eruption ENSO evolution and superpose SVE-induced climate variations according to the peak times of the eruptions. In this way, SVE signals can be highlighted within the complex ENSO evolutions. As shown in Fig. 16, the immediate eastern equatorial Pacific cooling is evident in July–October of the eruption year. Additionally, an extreme La Niña event can be found in the second half of the second post-eruption year and in the third post-eruption winter. Conversely, the interim El Niño-like warming is weak in the spring of the first post-eruption year. However, this El Niño-like response is significant in terms of the equatorial Pacific thermocline but not the SST. The thermocline deepens in the eastern equatorial Pacific due to the westerly wind anomalies (Fig. 17a, b). The SST characteristics of this El Niño-like process are most likely offset by strong cooling effects (Fig. 17c, d). At the same time, other tropical oceans are also significantly cooled by the volcanic forcing (Fig. 16). These characteristics imply that the modeled volcanic forcing might be too strong relative to that in reality. Therefore, how to realistically add volcanic forcing to the model will require further investigation.

In addition, we extend the reference period from the 5 pre-eruption years to the 30 pre-eruption years in our analysis. We obtain the same result (Figure S10), meaning that the conclusive ENSO evolution of the post-eruption years is not a simple positive or negative tendency based on its initial

state but is also an absolute ENSO phase transition relative to the long-term climatology.

In this study, we analyzed only the BCM EXT600 simulation. In fact, the ensemble simulation is the most suitable method for studying the volcanic effects on the climate system (e.g., Zanchettin et al. 2012; Pausata et al. 2015; Stevenson et al. 2017). To better understand the response of ENSO to volcanic forcing and the associated inter-model differences, additional analyses on ensemble simulations and multi-model simulations are needed.

Over the past few decades, the simulations and predictions of ENSO have been significantly improved (e.g., Latif et al. 1998; Zhang et al. 2003; Jin et al. 2008; Kumar et al. 2015). However, our predictions are still far from perfect due to the systematic biases in various components of coupled models (Zhu et al. 2013). Thus, many works must be performed to improve the current models. Moreover, better simulations and understandings of ENSO responses to external forcings are also necessary. By focusing on SVEs, we conclude that our results are beneficial to the post-eruption short-term predictions of ENSO and ENSO-related climates.

Acknowledgements We thank two anonymous reviewers and editor for their valuable comments and suggestions, which help to improve the quality of this paper significantly. This research was supported by the National Key R&D Program of China (Grant No. 2016YFA0600701), the National Natural Science Foundation of China (Grants 41575086, 41661144005, 41530423, and 41375072), and the CAS–PKU Joint Research Program. The authors are grateful to Dr Odd Helge Otterå for providing the coupled model (BCM) EXT600 simulation.

References

Adams JB, Mann ME, Ammann CM (2003) Proxy evidence for an El Nino-like response to volcanic forcing. Nature 426:274–278. https://doi.org/10.1038/nature02101

Anchukaitis KJ, Buckley BM, Cook ER, Cook BI, D'Arrigo RD, Ammann CM (2010) Influence of volcanic eruptions on the climate of the Asian monsoon region. Geophys Res Lett 37. https://doi.org/10.1029/2010GL044843

Andreoli RV, Kayano MT (2005) Enso-related rainfall anomalies in South America and associated circulation features during warm and cold Pacific Decadal Oscillation regimes. Int J Climatol 25:2017–2030. https://doi.org/10.1002/joc.1222

Ashok K, Behera SK, Rao SA, Weng H, Yamagata TJ (2007) El Niño Modoki and its possible teleconnection. J Geophys Res 112:C11007. https://doi.org/10.1029/2006JC003798

Battisti DS, Hirst AC (1989) Interannual variability in a tropical atmosphere ocean model—influence of the basic state, ocean geometry and nonlinearity. J Atmos Sci 46:1687–1712. https://doi.org/10.1175/1520-0469

Bjerknes J (1969) Atmospheric teleconnections from the equatorial Pacific. Mon Weather Rev 97:163–172

Bleck R, Rooth C, Hu DM, Smith LT (1992) Salinity-driven thermocline transients in a wind-forced and thermohaline-forced isopycnic coordinate model of the North-Atlantic. J Phys Oceanogr 22:1486–1505

Brönnimann S (2007) Impact of El Niño-Southern Oscillation on European climate. Rev Geophys 45:RG303. https://doi.org/10.1029/2006rg000199

Cai W, Cowan T (2009) La Nina Modoki impacts Australia autumn rainfall variability. Geophys Res Lett 36 https://doi.org/10.1029/2009gl037885

Cai WJ, van Rensch P, Cowan T, Hendon HH (2011) Teleconnection Pathways of ENSO and the IOD and the Mechanisms for Impacts on Australian Rainfall. J Clim 24:3910–3923. https://doi.org/10.1175/2011jcli4129.1

Cai WJ, Borlace S, Lengaigne M, van Rensch P, Collins M, Vecchi G, Timmermann A, Santoso A, McPhaden M, Wu LX, England MH, Wang GJ, Guilyardi E, Jin FF (2014) Increasing frequency of extreme El Niño events due to greenhouse warming. Nat Clim Change 4:111–116. https://doi.org/10.1038/nclimate2100

Cai WJ, Santoso A, Wang GJ, Yeh SW, An SI, Cobb KM, Collins M, Guilyardi E, Jin FF, Kug JS, Lengaigne M, McPhaden MJ, Takahashi K, Timmermann A, Vecchi G, Watanabe M, Wu LX (2015a) ENSO and greenhouse warming. Nat Clim Change 5(9):849–859

Cai WJ, Wang GJ, Santoso A, McPhaden MJ, Wu LX, Jin FF, Timmermann A, Collins M, Vecchi G, Lengaigne M, England MH, Dommenget D, Takahashi K, Guilyardi E (2015b) Increased frequency of extreme La Nina events under greenhouse warming. Nat Clim Change 5:132–137. https://doi.org/10.1038/Nclimate2492

Cane MA, Clement AC, Kaplan A, Kushnir Y, Pozdnyakov D, Seager R, Zebiak SE, Murtugudde R (1997) Twentieth-century sea surface temperature trends. Science 275:957–960

Capotondi A, Wittenberg A, Masina S (2006) Spatial and temporal structure of Tropical Pacific interannual variability in 20th century coupled simulations. Ocean Model 15:274–298. https://doi.org/10.1016/j.ocemod.2006.02.004

Cayan DR, Redmond KT, Riddle LG (1999) ENSO and hydrologic extremes in the western United States. J Clim 12:2881–2893. https://doi.org/10.1175/1520-0442

Chang CP, Zhang SY, Li T (2000) Interannual and interdecadal variations of the East Asian Summer Monsoon and Tropical Pacific SSTs. Part I: roles of the subtropical ridge. J Climate 13:4310–4325

Chavez FP, Strutton PG, Friederich CE, Feely RA, Feldman GC, Foley DC, McPhaden MJ (1999) Biological and chemical response of the equatorial Pacific Ocean to the 1997–98 El Nino. Science 286:2126–2131. https://doi.org/10.1126/science.286.5447.2126

Chen JM, Li T, Shih CF (2007) Fall persistence barrier of sea surface temperature in the South China Sea associated with ENSO. J Clim 20:158–172. https://doi.org/10.1175/Jcli4000.1

Chen L, Li T, Yu YQ (2015) Causes of strengthening and weakening of ENSO amplitude under global warming in four CMIP5 models. J Clim 28:3250–3274. https://doi.org/10.1175/Jcli-D-14-00439.1

Chen X, Ling J, Li CY (2016) Evolution of the Madden-Julian Oscillation in two types of El Nino. J Clim 29:1919–1934. https://doi.org/10.1175/Jcli-D-15-0486.1

Clement AC, Seager R, Cane MA, Zebiak SE (1996) An ocean dynamical thermostat. J Clim 9:2190–2196

Crowley TJ, Baum SK, Kim KY, Hegerl GC, Hyde WT (2003) Modeling ocean heat content changes during the last millennium. Geophys Res Lett 30 https://doi.org/10.1029/2003gl017801

Cui XD, Gao YQ, Sun JQ (2014) The response of the East Asian summer monsoon to strong tropical volcanic eruptions. Adv Atmos Sci 31:1245–1255. https://doi.org/10.1007/s00376-014-3239-8

Ding YN, Carton JA, Chepurin GA, Stenchikov G, Robock A, Sentman LT, Krasting JP (2014) Ocean response to volcanic eruptions in coupled model Intercomparison Project 5 simulations. J Geophys Res Oceans 119(9):5622–5637

Emile-Geay J, Seager R, Cane MA, Cook ER, Haug GH (2008) Volcanoes and ENSO over the Past Millennium. J Clim 21:3134–3148. https://doi.org/10.1175/2007jcli1884.1

Fraedrich K (1994) An ENSO impact on Europe? A review. Tellus A 46:541–552

Gent PR, and Coauthors (2011) The Community Climate System Model Version 4. J Clim 24:4973–4991

Giese BS, Ray S (2011) El Nino variability in simple ocean data assimilation (SODA), 1871–2008. J Geophys Res Oceans 116(C2):C02024. https://doi.org/10.1029/2010JC006695

Gill AE (1980) Some simple solutions for heat-induced tropical circulation. Quart J Roy Meteor Soc 106:447–462

Graf HF (1986) El-Nino southern oscillation and northern hemispheric temperature. Gerlands Beitr Geophysik 1:63–75

Graf HF, Zanchettin D, Timmreck C, Bittner M (2014) Observational constraints on the tropospheric and near-surface winter signature of the Northern Hemisphere stratospheric polar vortex. Clim Dynam 43:3245–3266

Gu DJ, Li T, Ji ZP, Zheng B (2010) Connection of the South China Sea Summer Monsoon to Maritime Continent Convection and Enso. J Trop Meteorol 16:1–9. https://doi.org/10.3969/j.issn.1006-8775.2010.01.001

He YC, Drange H, Gao YQ, Bentsen M (2016) Simulated Atlantic Meridional Overturning Circulation in the 20th century with an ocean model forced by reanalysis-based atmospheric data sets. Ocean Model 100:31–48

Jin FF (1997a) An equatorial ocean recharge paradigm for ENSO .1. Conceptual model. J Atmos Sci 54:811–829. https://doi.org/10.1175/1520-0469

Jin FF (1997b) An equatorial ocean recharge paradigm for ENSO .2. A stripped-down coupled model. J Atmos Sci 54:830–847. https://doi.org/10.1175/1520-0469

Jin EK et al (2008) Current status of ENSO prediction skill in coupled ocean-atmosphere models. Clim Dynam 31:647–664. https://doi.org/10.1007/s00382-008-0397-3

Johnson NC (2013) How Many ENSO Flavors Can We Distinguish? J Clim 26:4816–4827

Kalnay E et al (1996) The NCEP/NCAR 40-year reanalysis project. B Am Meteorol Soc 77:437–471

Kao HY, Yu JY (2009) Contrasting Eastern-Pacific and Central-Pacific types of ENSO. J Clim 22:615–632. https://doi.org/10.1175/2008JCLI2309.1

Khodri M, Izumo T, Vialard J, Janicot S, Cassou C, Lengaigne M, Mignot J, Gastineau G, Guilyardi E, Lebas N, Robock A, Mcphaden MJ (2017) Tropical explosive volcanic eruptions can trigger El Niño by cooling tropical Africa. Nat Commun 8:778. https://doi.org/10.1038/s41467-017-00755-6

Kosaka Y, Xie SP (2013) Recent global-warming hiatus tied to equatorial Pacific surface cooling. Nature 501:403–407. https://doi.org/10.1038/nature12534

Kug JS, Li T, An SI, Kang IS, Luo JJ, Masson S, Yamagata T (2006) Role of the ENSO-Indian Ocean coupling on ENSO variability in a coupled GCM. Geophys Res Lett 33 https://doi.org/10.1029/2005gl024916

Kumar A, Chen MY, Xue Y, Behringer D (2015) An Analysis of the temporal evolution of ENSO prediction skill in the context of the Equatorial Pacific Ocean observing system. Mon Weather Rev 143:3204–3213. https://doi.org/10.1175/Mwr-D-15-0035.1

Lai AW, Herzog M, Graf HF (2015) Two key parameters for the El Niño continuum: zonal wind anomalies and Western Pacific subsurface potential temperature. Clim Dynam 45:3461–3480

Latif M et al (1998) A review of the predictability and prediction of ENSO. J Geophys Res-Oceans 103:14375–14393. https://doi.org/10.1029/97jc03413

Lewis MR, Carr ME, Feldman GC, Esaias W, Mcclain C (1990) Influence of penetrating solar-radiation on the heat-budget of the Equatorial Pacific-Ocean. Nature 347:543–545. https://doi.org/10.1038/347543a0

Li JB, Xie SP, Cook ER, Morales MS, Christie DA, Johnson NC, Chen FH, D'Arrigo R, Fowler AM, Gou XH, Fang KY (2013) El Nino modulations over the past seven centuries. Nat Clim Change 3(9):822–826

Lim H-G, Yeh S-W, Kug J-S, Park Y-G, Park J-H, Park R, Song C-K (2016) Threshold of the volcanic forcing that leads the El Niño-like warming in the last millennium: results from the ERIK simulation. Clim Dynam 46:3725–3736. https://doi.org/10.1007/s00382-015-2799-3

Liu F, Chai J, Huang G, Liu J, Chen ZY (2015) Modulation of decadal ENSO-like variation by effective solar radiation. Dynam Atmos Oceans 72:52–61. https://doi.org/10.1016/j.dynatmoce.2015.10.003

Liu F, Chai J, Wang B, Liu J, Zhang X, Wang ZY (2016) Global monsoon precipitation responses to large volcanic eruptions. Sci Rep https://doi.org/10.1038/srep24331

Liu F, Li JB, Wang B, Liu J, Li T, Huang G, Wang ZY (2017) Divergent El Niño responses to volcanic eruptions at different latitudes over the past millennium. Clim Dynam. https://doi.org/10.1007/s00382-017-3846-z

Maher N, McGregor S, England MH, Sen Gupta A (2015) Effects of volcanism on tropical variability. Geophys Res Lett 42:6024–6033. https://doi.org/10.1002/2015gl064751

Mann ME, Cane M, Zebiak SE, Clement A (2005) Volcanic and Solar Forcing of the Tropical Pacific over the Past 1000 Years. J Clim 18:447–456

Marzeion B, Timmermann A, Murtugudde R, Jin FF (2005) Biophysical feedbacks in the tropical Pacific. J Clim 18:58–70. https://doi.org/10.1175/Jcli3261.1

Matsuno T (1966) Quasi-geostrophic motions in the equatorial area. J Meteor Soc Jpn 44:25–43

McGregor S, Timmermann A (2011) The Effect of Explosive Tropical Volcanism on ENSO. J Clim 24:2178–2191. https://doi.org/10.1175/2010jcli3990.1

McPhaden MJ, Yu X (1999) Equatorial waves and the 1997–98 El Nino. Geophys Res Lett 26:2961–2964

McPhaden MJ, Zebiak SE, Glantz MH (2006) ENSO as an integrating concept in Earth science. Science 314:1740–1745. https://doi.org/10.1126/science.1132588

Miao J, Wang T, Zhu Y, Min J, Wang H, Guo D (2016) Response of the East Asian Winter Monsoon to Strong Tropical Volcanic Eruptions. J Clim 29:5041–5057. https://doi.org/10.1175/jcli-d-15-0600.1

Mitchell JM (1961) Recent secular changes of the global temperature. Ann N Y Acad Sci 95:235–250. https://doi.org/10.1111/j.1749-6632.1961.tb50036.x

Moron V, Plaut G (2003) The impact of El Nino-southern oscillation upon weather regimes over Europe and the North Atlantic during boreal winter. Int J Climatol 23:363–379. https://doi.org/10.1002/joc.890

Neelin JD, Battisti DS, Hirst AC, Jin FF, Wakata Y, Yamagata T, Zebiak SE (1998) ENSO theory. J Geophys Res-Oceans 103:14261–14290

Newman M, Compo GP, Alexander MA (2003) ENSO-forced variability of the Pacific decadal oscillation. J Clim 16:3853–3857. https://doi.org/10.1175/1520-0442

Ohba M, Shiogama H, Yokohata T, Watanabe M (2013) Impact of Strong Tropical Volcanic Eruptions on ENSO Simulated in a Coupled GCM. J Clim 26:5169–5182. https://doi.org/10.1175/Jcli-D-12-00471.1

Otterå OH (2008) Simulating the effects of the 1991 Mount Pinatubo volcanic eruption using the ARPEGE atmosphere general circulation model. Adv Atmos Sci 25:213–226. https://doi.org/10.1007/s00376-008-0213-3

Otterå OH, Bentsen M, Drange H, Suo LL (2010) External forcing as a metronome for Atlantic multidecadal variability. Nat Geosci 3:688–694. https://doi.org/10.1038/Ngeo955

Pascolini-Campbell M, Zanchettin D, Bothe O, Timmreck C, Matei D, Jungclaus JH, Graf HF (2015) Toward a record of Central Pacific El Niño events since 1880. Theor Appl Climatol 119:379–389

Pausata FS, Chafik L, Caballero R, Battisti DS (2015) Impacts of high-latitude volcanic eruptions on ENSO and AMOC. Proc Natl Acad Sci USA 112:13784–13788

Pausata FS, Karamperidou C, Caballero R, Battisti DS (2016) ENSO response to high-latitude volcanic eruptions in the Northern Hemisphere: the role of the initial conditions. Geophys Res Lett 43:8694–8702

Peng YB, Shen CM, Wang WC, Xu Y (2010) Response of summer precipitation over Eastern China to large volcanic eruptions. J Clim 23:818–824. https://doi.org/10.1175/2009jcli2950.1

Picaut J, Masia F, duPenhoat Y (1997) An advective-reflective conceptual model for the oscillatory nature of the ENSO. Science 277:663–666. https://doi.org/10.1126/science.277.5326.663

Picaut J, Hackert E, Busalacchi AJ, Murtugudde R, Lagerloef GSE (2002) Mechanisms of the 1997–1998 El Nino La Nina, as inferred from space-based observations. J Geophys Res-Oceans. https://doi.org/10.1029/2001jc000850

Rasmusson EM, Carpenter TH (1982) Variation in tropical sea surface temperature and surface wind fields associated with Southern Oscillation/El Niño. Mon Weather Rev 110:354–384

Rayner NA et al. (2003) Global analyses of sea surface temperature, sea ice, and night marine air temperature since the late nineteenth century. J Geophys Res-Atmos. https://doi.org/10.1029/2002jd002670

Robock A (2000) Volcanic eruptions and climate. Rev Geophys 38:191–219. https://doi.org/10.1029/1998rg000054

Robock A, Mao JP (1995) The volcanic signal in surface-temperature observations. J Clim 8:1086–1103. https://doi.org/10.1175/1520-0442

Salas-Melia D (2002) A global coupled sea ice-ocean model. Ocean Model 4:137–172

Stenchikov GL et al (1998) Radiative forcing from the 1991 Mount Pinatubo volcanic eruption. J Geophys Res Atmos 103:13837–13857. https://doi.org/10.1029/98jd00693

Stevenson S, Otto-Bliesner B, Fasullo J, Brady E (2016) "El Nino Like" hydroclimate responses to last millennium volcanic eruptions. J Clim 29:2907–2921

Stevenson S, Fasullo JT, Otto-Bliesner BL, Tomas RA, Gao CC (2017) Role of eruption season in reconciling model and proxy responses to tropical volcanism. P Natl Acad Sci USA 114:1822–1826

Suarez MJ, Schopf PS (1988) A Delayed action oscillator for Enso. J Atmos Sci 45:3283–3287. https://doi.org/10.1175/1520-0469

Timmermann A, Jin FF (2002) Phytoplankton influences on tropical climate. Geophys Res Lett 29 https://doi.org/10.1029/2002gl015434

Trenberth KE, Dai A (2007) Effects of Mount Pinatubo volcanic eruption on the hydrological cycle as an analog of geoengineering. Geophys Res Lett 34 https://doi.org/10.1029/2007gl030524

Vecchi GA, Soden BJ, Wittenberg AT, Held IM, Leetmaa A, Harrison MJ (2006) Weakening of tropical Pacific atmospheric circulation due to anthropogenic forcing. Nature 441:73–76. https://doi.org/10.1038/nature04744

Wang CZ, Picaut J (2004) Understanding ENSO physics-A review. Earth's Climate, vol Geophysical Monograph Series. American Geophysical Union

Wang CZ, Weisberg RH, Virmani JI (1999) Western Pacific interannual variability associated with the El Nino Southern oscillation. J Geophys Res Oceans 104:5131–5149. https://doi.org/10.1029/1998jc900090

Wang T, Ottera OH, Gao YQ, Wang HJ (2012) The response of the North Pacific Decadal Variability to strong tropical volcanic eruptions. Clim Dynam 39:2917–2936. https://doi.org/10.1007/s00382-012-1373-5

Wang T, Wang HJ, Ottera OH, Gao YQ, Suo LL, Furevik T, Yu L (2013) Anthropogenic agent implicated as a prime driver of shift in precipitation in eastern China in the late 1970s. Atmos Chem Phys 13:12433–12450. https://doi.org/10.5194/acp-13-12433-2013

Weisberg RH, Wang CZ (1997) A western Pacific oscillator paradigm for the El Nino Southern Oscillation. Geophys Res Lett 24:779–782. https://doi.org/10.1029/97gl00689

Yang S, Lau KM, Schopf PS (1999) Sensitivity of the tropical Pacific Ocean to precipitation induced freshwater flux. Clim Dynam 15:737–750. https://doi.org/10.1007/s003820050313

Zambri B, Robock A (2016) Winter warming and summer monsoon reduction after volcanic eruptions in Coupled Model Intercomparison Project 5 (CMIP5) simulations. Geophys Res Lett 43:10920–10928

Zanchettin D (2017) Aerosol and solar irradiance effects on decadal climate variability and predictability. Current Climate Change Reports 3:150. https://doi.org/10.1007/s40641-017-0065-y

Zanchettin D et al (2012) Bi-decadal variability excited in the coupled ocean-atmosphere system by strong tropical volcanic eruptions. Clim Dynam 39:419–444. https://doi.org/10.1007/s00382-011-1167-1

Zanchettin D, Bothe O, Rubino A, Jungclaus JH (2016) Multi-model ensemble analysis of Pacific and Atlantic SST variability in unperturbed climate simulations. Clim Dynam 47:1073–1090

Zebiak SE, Cane MA (1987) A model El Niño/Southern Oscillation. Mon Wea Rev 115:2262–2278

Zhang RH, Busalacchi AJ (2009) Freshwater flux (FWF)-induced Oceanic feedback in a hybrid coupled model of the Tropical Pacific. J Clim 22:853–879. https://doi.org/10.1175/2008jcli2543.1

Zhang RH, Akimasa S, Masahide K (1999) A Diagnostic Study of the Impact of El Niño on the Precipitation in China. Adv Atmos Sci 16:229–241

Zhang RH, Zebiak SE, Kleeman R, Keenlyside N (2003) A new intermediate coupled model for El Niño simulation and prediction. Geophys Res Lett 30 https://doi.org/10.1029/2003gl018010

Zhang Q, Kumar A, Xue Y, Wang WQ, Jin FF (2007) Analysis of the ENSO cycle in the NCEP coupled forecast model. J Climate 20:1265–1284. https://doi.org/10.1175/Jcli4062.1

Zhang RH, Gao C, Kang XB, Zhi H, Wang ZG, Feng LC (2015) ENSO Modulations due to Interannual Variability of Freshwater Forcing and Ocean Biology-induced Heating in the Tropical Pacific. Sci Rep https://doi.org/10.1038/srep18506

Zheng F (2014) ENSO variability simulated by a coupled general circulation model: ECHAM5/MPI-OM. Atmos Ocean Sci Lett 7:471–475

Zheng F, Zhang RH (2012) Effects of interannual salinity variability and freshwater flux forcing on the development of the 2007/08 La Nina event diagnosed from Argo and satellite data. Dynam Atmos Oceans 57:45–57. https://doi.org/10.1016/j.dynatmoce.2012.06.002

Zheng F, Zhu J (2015) Observed splitting eastbound propagation of subsurface warm water over the equatorial Pacific in early 2014. Sci Bull 60:477–482. https://doi.org/10.1007/s11434-014-0678-7

Zhou W, Chan JCL (2007) ENSO and the South China Sea summer monsoon onset. Int J Climatol 27:157–167. https://doi.org/10.1002/joc.1380

Zhou W, Wang X, Zhou TJ, Chan JCL (2007) Interdecadal variability of the relationship between the East Asian winter monsoon and ENSO. Meteorol Atmos Phys 98:283–293. https://doi.org/10.1007/s00703-007-0263-6

Zhu JS, Zhou GQ, Zhang RH, Sun ZB (2013) Improving ENSO prediction in a hybrid coupled model with an embedded entrainment temperature parameterisation. Int J Climatol 33:343–355. https://doi.org/10.1002/joc.3426

Affiliations

Tao Wang[1,2] · Dong Guo[3] · Yongqi Gao[1,4] · Huijun Wang[1,2,5] · Fei Zheng[2,6] · Yali Zhu[1,2] · Jiapeng Miao[1,7] · Yongyun Hu[8]

1 Nansen-Zhu International Research Centre, Institute of Atmospheric Physics, Chinese Academy of Sciences, Beijing 100029, China

2 Collaborative Innovation Center on Forecast and Evaluation of Meteorological Disasters, Nanjing University of Information Science and Technology, Nanjing 210044, China

3 Climate Change Research Center, Chinese Academy of Sciences, Beijing 100029, China

4 Nansen Environmental and Remote Sensing Center/Bjerknes Centre for Climate Research, Bergen, Norway

5 Key Laboratory of Meteorological Disaster, Nanjing University of Information Science and Technology, Nanjing 210044, China

6 International Center for Climate and Environment Science, Institute of Atmospheric Physics, Chinese Academy of Sciences, Beijing 100029, China

7 University of Chinese Academy of Sciences, Beijing, China

8 Laboratory for Climate and Ocean-Atmosphere Sciences, Department of Atmospheric and Oceanic Sciences, School of Physics, Peking University, Beijing 100871, China